

Industrial Anomaly Detection and Localization Using Weakly-Supervised Residual Transformers

Hanxi Li^{1,2,†}, Jingqi Wu^{1,2,†}, Lin Yuanbo Wu^{3,*}, Hao Chen², Mingwen Wang¹, and Chunhua Shen^{2,*}

¹*Jiangxi Normal University, Jiangxi, China*

²*Zhejiang University, Zhejiang, China*

³*Swansea University, United Kingdom*

[†]*These authors contributed equally to this work*

^{*}*Corresponding authors*

arXiv:2306.03492v4 [cs.CV] 8 Jul 2024

Abstract—Recent advancements in industrial Anomaly Detection (AD) have shown that incorporating a few anomalous samples during training can significantly boost accuracy. However, this performance improvement comes at a high cost: extensive annotation efforts, which are often impractical in real-world applications. In this work, we propose a novel framework called “Weakly-supervised RESidual Transformer” (WeakREST), which aims to achieve high AD accuracy while minimizing the need for extensive annotations. First, we reformulate the pixel-wise anomaly localization task into a block-wise classification problem. By shifting the focus to block-wise level, we can drastically reduce the amount of required annotations without compromising on the accuracy of anomaly detection. Secondly, we design a residual-based transformer model, termed “Positional Fast Anomaly Residuals” (PosFAR), to classify the image blocks in real time. We further propose to label the anomalous regions using only bounding boxes or image tags as weaker labels, leading to a semi-supervised learning setting.

On the benchmark dataset MVTec-AD, our proposed WeakREST framework achieves a remarkable Average Precision (AP) of 83.0%, significantly outperforming the previous best result of 75.8% in the unsupervised setting. In the supervised AD setting, WeakREST further improves performance, attaining an AP of 87.6% compared to the previous best of 78.6%. Notably, even when utilizing weaker labels based on bounding boxes, WeakREST surpasses recent leading methods that rely on pixel-wise supervision, achieving an AP of 87.1% against the prior best of 78.6% on MVTec-AD. This precision advantage is also consistently observed on other well-known AD datasets, such as BTAD and KSD2. Code is available at: https://github.com/BeJane/Semi_REST

Index Terms—Anomaly detection, Weakly supervised segmentation, Semi-supervised learning.

I. INTRODUCTION

Product quality control is crucial in many manufacturing processes. Manual inspection is expensive and unreliable considering the limited time budget for inspection on a running assembly line. As a result, automatic defect inspection is in great demand in modern manufacturing industries [1]–[4]. Given training samples with sufficient supervision, it is straightforward to perform defect detection using off-the-shelf detection or segmentation algorithms [5]–[8]. Unfortunately, in most practical cases, one can only obtain much fewer

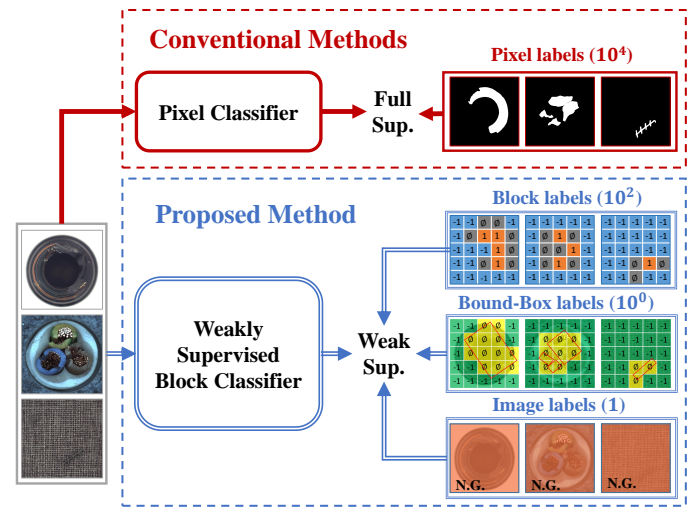


Fig. 1. The comparison between the proposed weak labels with the conventional paradigm. Different from the traditional pixel-wise labels (red box on the top), the proposed annotations can be divided into three levels, as shown in the three rows on the bottom blue box. Row-1: solving the AD problem as block-wise binary classifications with the normal samples, anomalous samples, and ignored ones shown in blue, orange, and gray respectively; Row-2: the weaker label based on bonding boxes which covering the entire anomalous region. Row-3: the weakest label using only tags indicating the defective status of the image. The numbers in the parenthesis denote the order of magnitudes (from 10^4 to 1) of the annotation clicks under the three levels of weak annotations. Best viewed in color.

“anomalous” samples than the normal ones and the anomaly pattern varies dramatically over different samples.

To address this difficulty, the industrial defect detection task is often cast into an Anomaly Detection (AD) problem [9], [10], with only normal instances available for training. This supervision condition is usually referred to as the “unsupervised” setting and has attracted much attention from the computer vision community. In specific, the most straightforward way of realizing AD is to treat the normal image patches as one class while the anomalous ones as outliers [11]–[17]. Some researchers propose to localize the anomalies by comparing the test image patches with the normal references which are directly captured from the training set [18]–[23] or reconstructed based on the normal samples [24]–[28]. Besides, the distillation-based methods [29]–[32] and latent

This work was conducted during Hanxi Li’s visit to Zhejiang University.

image registration [33], [34] are also proposed to enhance the outlier effect of anomalies.

Despite the mainstream “unsupervised” fashion, in [35]–[37], anomaly detectors are trained in a “supervised” manner and unsurprisingly higher performances are achieved. Actually, the traditional surface defect detection tasks [38]–[41] are also solved with manually labeled defects. Considering that in practice, a few abnormal samples are not difficult to obtain, especially in the “warming-up” stage of the assembly lines, this “supervised” setting is usually valid.

In this paper, we claim that, compared with the lack of training anomalies, a more realistic problem to address is the limited time budget for labeling the newly-obtained anomalous images. Accordingly, we propose a novel AD algorithm that simultaneously enjoys high detection robustness and low annotation cost. The high-level concept of the proposed algorithm is illustrated in Fig 1.

In specific, we consider the AD task as a block-wise classification problem (as shown in right-bottom part of Fig 1) and thus one only needs to label hundreds of anomaly blocks instead of thousands of anomaly pixels on a defective image. A faster and better residual generation algorithm termed “Positional Fast Anomaly Residuals” (PosFAR), is proposed to generate features for each image block. The image block are then classified into anomalous or normal by a Swin Transformer [42] model. Thanks to the novel features and the customized training scheme, the proposed algorithm performs better than the existing methods with pixel-level supervision. In addition, we propose a new foreground estimation method to further increase the AD performance in the scenario of examining the defects on objects.

More aggressively, we propose to further reduce the annotation cost by labeling the anomaly regions with only bounding boxes or even image tags. As can be seen in the row-3 and row-4 of the right part of Fig 1, the boxes cover all the anomaly regions so the outside blocks (shown in green) can be directly used as normal samples in training. On the other hand, the inside blocks (shown in yellow), though labeled as “unknown”, can be utilized effectively via a novel semi-supervised learning algorithm that is customized for our transformer-based anomaly detector. The productive utilization of the unlabeled information maintain the high AD performance of our method with the “cheaper” labels.

We term the proposed AD algorithm “Weakly-supervised RESidual Transformer” or “WeakREST” in short. The experiments in this paper verify the superiority of the proposed method: WeakREST outperforms all the state-of-the-art AD algorithms on the three well-known datasets (MVTec-AD [9], BTAD [10] and KSDD2 [41]) in both the mainstream “unsupervised” setting and the “supervised” setting. In addition, with only bounding-box annotations, the WeakREST also beats all the SOTA methods supervised by pixel labels, with all the employed evaluation metrics. In summary, our main contribution is three fold, as listed below.

- **Cheaper in terms of annotation:** From a realistic perspective, we suggest that, compared with the “one-class” compatibility, a more desirable property for AD algorithms is the high efficiency of using annotation infor-

mation. Accordingly, this work proposes several kinds of low-cost annotations: the block-wise labels, the bounding box labels and the image-level labels **To the best of our knowledge, it is the first time that the block-wise label is used for anomaly detection and the usage of the bounding-box label and image tags is also creative in the literature of AD.**

- **Better in terms of accuracy:** We design the WeakREST algorithm based on a modified Swin-Transformer [42]; a novel residual generation algorithm PosFAR, and an effective foreground estimation algorithm for the object-oriented AD tasks. **The proposed algorithm consistently surpasses the SOTA methods by large margins, on the three most acknowledged datasets and in all the supervision conditions.**
- **Cheaper and Better:** Given the cheap bounding-box or image-level labels, WeakREST can effectively utilize the unlabeled features thanks to the proposed *ResMixMatch* algorithm, which is inspired by the MixMatch [43] algorithm but highly customized for transformer models with residual inputs. **Simply using these lightweight annotations, WeakREST still outperforms all the comparing SOTA methods trained with pixel labels.**

The remaining part of this paper is organized as follows: Sec. II introduces the background knowledge and related work of this paper; readers can find the detailed introduction of the proposed method in Sec. III; all the settings and results of the experiments conducted in this paper can be found in Sec. IV; Sec. V is the conclusion section.

II. RELATED WORK

A. Two supervision conditions in Industrial Anomaly Detection

1) Unsupervised Setting

In the conventional setting of industrial anomaly detection tasks, all the training samples are anomaly-free and the defective patterns are detected as outliers in the test phase [11]–[17], [44]–[48]. This setting is usually referred to as “unsupervised” in the AD literature even though mild supervision, *i.e.* the anomaly-free labels, still exist in the training set. To learn a discriminative model in this supervision condition, some sophisticated algorithms propose to generate artificial anomalous samples with synthetic defective regions [32], [49]–[51] for higher AD accuracy.

2) Supervised Setting

Encouraged by the success of the AD models based on synthetic defects, some recently proposed methods [35]–[37] involve a few genuine anomalous samples to further unleash the discriminative power. They term this new setting as “supervised” in contrast to the default “unsupervised” setting. Note that in this supervision condition, the original anomaly-free samples as well as the fake defects are also employed in training.

In this work, we propose to replace the original pixel-level annotations with weak labels to reduce the annotation cost

fundamentally. We term this supervision condition as “weakly-supervised” and design a novel algorithm for leveraging the weak labels to achieve even superior performance than the existing algorithms within the fully supervised condition.

B. Path-Matching-based AD Algorithms

As a simple and typical example of the patch-matching-based AD methods, PatchCore algorithm [18] proposes the coresnet-subsampling algorithm to build a “memory bank” of patch features, which are obtained via smoothing the neutral deep features pre-learned on ImageNet [52], [53]. The anomaly score is then calculated based on the Euclidean distance between the test patch feature and its nearest neighbor in the “memory bank”. Despite the simplicity, PatchCore performs dramatically well on the MVTec-AD dataset [9].

The good performance of PatchCore encourages researchers to develop better variants based on it. The PAFM algorithm [19] applies patch-wise adaptive coresnet sampling to improve the speed. [20] introduces the position and neighborhood information to refine the patch-feature comparison. Graphcore [23] utilizes graph representation to customize PatchCore for the few-shot setting. [21] modifies PatchCore by compressing the memory bank via k-means clustering. [22] combines PatchCore [18] and Defect GAN [54] for higher AD performances. Those variants, though achieving slightly better performances, all fail to notice the potential value of the intermediate information generated by the patch-matching. In this work, we use the matching residuals as the input tokens of our transformer model. The individual and the mutual information of the residuals are effectively exploited and new SOTA performances are then obtained.

C. Swin Transformer for Anomaly Detection

As a variation of Vision Transformer (ViT) [55], Swin Transformer [42], [56] proposed a hierarchical Transformer with a shifted windowing scheme, which not only introduces several visual priors into Transformer but also reduces computation costs. Swin Transformer and its variants illustrate remarkable performances in various computer vision tasks, such as semantic segmentation [57]–[59], instance segmentation [60]–[62] and object detection [63]–[65].

In the literature on anomaly detection, some recently proposed methods also employ Swin Transformer as the backbone network. [66] develops a hybrid structure decoder that combines convolution layers and the Swin Transformer. [67] improves the original shifted windowing scheme of the Swin Transformer for surface defect detection. Despite the success of Swin Transformer models in other domains, the Swin-Transformer-based AD algorithms could hardly outperform the SOTA methods on most acknowledged datasets such as [9], [10] and [41].

In this paper, we successfully tame the Swin Transformer for the small training sets of AD problems by introducing a series of novel modifications.

D. MixMatch and Weak Labels Based on Bounding Boxes

Semi-supervised Learning (SSL) is attractive since it saves massive labeling labor. Many efforts have been devoted to utilizing the information from the unlabeled data [43], [68]–[72], mainly focusing on the generation of high-quality pseudo labels. Inspired by the seminar work [73], [74] for data augmentation, MixMatch proposes a single-loss SSL method that relies on a smart fusion process between labeled and unlabeled samples and thus enjoys high accuracy and simplicity.

On the other hand, in the literature on semantic segmentation, bounding boxes are usually used as weak supervision to save labeling costs. [75] exploits the tightness prior to the bounding boxes to generate the positive and negative bags for multiple instance learning (MIL). [76] integrates the tightness prior and a global background emptiness constraint derived from bounding box annotations into a weak semantic segmentation of medical images. [77] propose a bounding box attribution map (BBAM) to produce pseudo-ground-truth for weakly supervised semantic and instance segmentation.

In this work, within the block-wise classification framework, MixMatch is smartly tailored to exploit the information of unlabeled blocks which are brought by the weak supervision of bounding boxes. This combination of the novel semi-supervised learning scheme and the bounding box labels is remarkably effective according to the experiment results and also novel in the literature, to our best knowledge.

III. OUR PROPOSED METHOD

A. Overview of the Algorithm

The overall inference process of our WeakREST algorithm is illustrated in Fig 2. As can be seen, there are four stages in the whole process: the novel feature extracting stage and the PosFAR generation stage (the gray box and blue box), which are introduced in Sec. III-B; the defect classification process based on a Swin Transformer model (the orange box), which is defined in Sec. III-C and a post-process for foreground estimation (the green box) whose description can be found in Sec. III-E.

B. PosFAR: Fast Anomaly Residuals with Position Constraints

1) *Matching Residual for Anomaly Detection*: Mathematically, for a input image $I \in \mathbb{R}^{h_1 \times w_1 \times 3}$, one can extract deep features as

$$[\mathbf{f}_1, \mathbf{f}_2, \dots, \mathbf{f}_M] \leftarrow \text{Flatten} \leftarrow \mathbf{F} = \Psi_{\text{CNN}}(I) \quad (1)$$

where $\Psi_{\text{CNN}}(\cdot)$ represents a deep network, which is pre-trained on a large but neutral dataset (ImageNet [53] for example); $\mathbf{F} \in \mathbb{R}^{h_f \times w_f \times d_f}$ denotes the generated deep feature tensor with M feature vectors ($M = h_f \cdot w_f$); $\mathbf{f}_i \in \mathbb{R}^{d_f}, i = 1, 2, \dots, M$ stands for the i -th deep feature vector extracted from the tensor \mathbf{F} . One then can build the memory “bank” of the defect-free training set as

$$\mathcal{B}_{\text{raw}} = \{\mathbf{f}_{i,j}^{\text{ref}} \in \mathbb{R}^{d_f} \mid \forall j = 1, \dots, N_{\text{trn}}, \forall i = 1, \dots, M\} \quad (2)$$

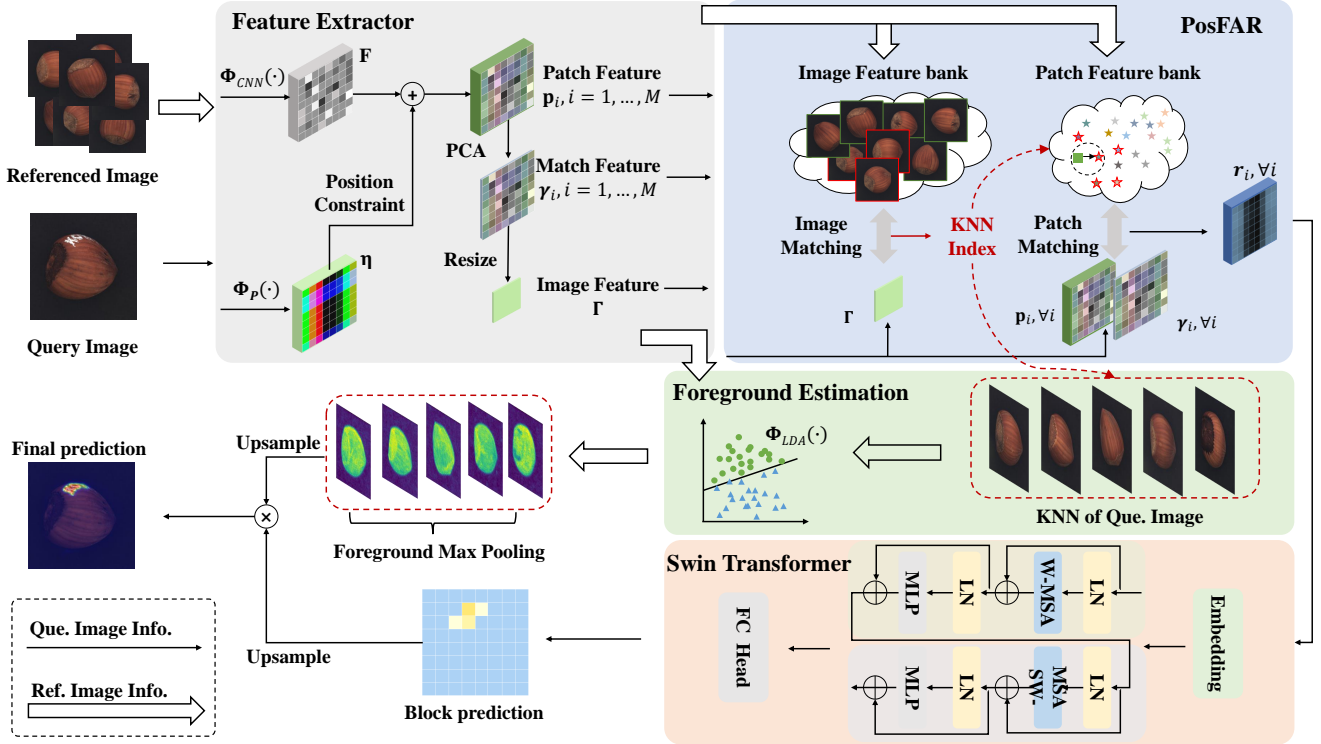


Fig. 2. The overview of the inference process of WeakREST. There are four modules of the proposed method: the novel feature extracting method (see Sec. III-B); the PosFAR residual generator (see Sec. III-B); the Swin Transformer module for block-wise anomaly classification (see Sec. III-C) and the foreground estimation module (see Sec. III-E). In this residual-based AD algorithm, the query and reference information are manipulated cooperatively in the entire process.

where N_{trn} denotes the number of training images. \mathcal{B}_{raw} contains $M \cdot N_{trn}$ feature vectors and is usually further down sampled as

$$\mathcal{B} = \Psi_{core}(\mathcal{B}_{raw}) = \{\mathbf{f}_t^{ref} \in \mathbb{R}^{d_f} \mid \forall t = 1, \dots, T\} \quad (3)$$

where $\Psi_{core}(\cdot)$ represents the “coreset” sampling scheme proposed in [18], and $T \ll M \cdot N_{trn}$ for decreasing the matching complexity. Then a test patch feature \mathbf{f}_i^{tst} is matched with the reference features in \mathcal{B} as

$$t^* = \arg \min_{\forall t=1, \dots, T} \|\mathbf{f}_i^{tst} - \mathbf{f}_t^{ref}\|_{l_2}. \quad (4)$$

The corresponding minimal distance $d_i = \|\mathbf{f}_i^{tst} - \mathbf{f}_{t^*}^{ref}\|_{l_2}$ is usually used to calculate the anomaly score of the test patch [18]–[21].

However, this vanilla version of patch matching suffers from some drawbacks, such as serious but unnecessary information loss, low efficiency, and ignorance of patch locations. In this work, We thus design a more sophisticated patch matching scheme and term the yielded residual feature “Positional Fast Anomaly Residuals” (PosFAR), as introduced in the following.

2) *Position Constrained Features*: Recently, new evidences show that, the positional information of the comparing patches could improve the AD performance [20], [78]. Accordingly, we borrow the “positional embedding” concept from the literature of Transformers [42], [55] to patch matching: the original patch features are aggregated with their positional features encoded in the Transformer way [79]. Mathematically, given a patch feature \mathbf{f} defined in Eq. 1, we generate its

“position-constrained” version as

$$\mathbf{p} = \mathbf{f} + \lambda_P \boldsymbol{\eta} = \mathbf{f} + \lambda_P \Phi_P(r, c) \quad (5)$$

where $\boldsymbol{\eta} = \Phi_P(r, c) \in \mathbb{R}^{d_f}$ is usually termed Position Code in the literature [79], with the row-column coordinate $[r, c]$ of \mathbf{f} extracted from the feature tensor $\mathbf{F} \in \mathbb{R}^{h_f \times w_f \times d_f}$. The function $\Phi_P(\cdot)$ denotes the positional embedding process that calculates the k -th element of $\boldsymbol{\eta}$ as

$$\eta_k = \begin{cases} \sin\left(\frac{c}{10000^{8k/d_f}}\right) & k \in [0, \frac{d_f}{4}) \\ \cos\left(\frac{c}{10000^{8(k-d_f/4)/d_f}}\right) & k \in [\frac{d_f}{4}, \frac{d_f}{2}) \\ \sin\left(\frac{r}{10000^{8(k-d_f/2)/d_f}}\right) & k \in [\frac{d_f}{2}, \frac{3d_f}{4}) \\ \cos\left(\frac{r}{10000^{8(3d_f/4)/d_f}}\right) & k \in [\frac{3d_f}{4}, d_f) \end{cases} \quad (6)$$

where $k \in [1, d_f]$, $r \in [1, h_f]$, $c \in [1, w_f]$. In this way, the whole patch feature matching process is constrained by the positional information and the new patch feature is termed “Position Constrained Feature” (PCF) in this work. The ablation study in Section IV-F verifies the merit of this constraint.

3) *Matching in a Lower Dimensional Space*: The conventional patch matching process is slow and thus can hardly be employed in practice. Consequently, we propose a novel algorithm to generate the anomaly residuals faster while maintaining their discriminative property. Firstly, the patch matching is performed in a lower-dimensional space. A Principle Component Analysis (PCA) is conducted over the PCFs extracted from the training set and then a PCF $\mathbf{p} \in \mathbb{R}^{d_f}$ is

mapped to an lower-dimensional space as

$$\gamma = \Psi_{\text{PCA}}(\mathbf{p}) = \mathbf{W}_{\text{PCA}}(\mathbf{p} - \mu_{\text{PCA}}) \in \mathbb{R}^{d_l}, \quad (7)$$

where $d_l \ll d_f$ denotes the lower dimension, $\mathbf{W}_{\text{PCA}} \in \mathbb{R}^{d_l \times d_f}$ and $\mu_{\text{PCA}} \in \mathbb{R}^{d_f}$ stand for the PCA mapping matrix and the mean feature vector respectively, $\gamma \in \mathbb{R}^{d_l}$ denotes the feature for faster patch matching. In this way, one can convert the bank \mathcal{B} defined in Eq. 3 into its position-constrained and lower-dimensional version as

$$\mathcal{B}_{\text{raw}} \xrightarrow{+\lambda_P \eta} \mathcal{B}_{\text{raw}}^P \xrightarrow{\Psi_{\text{core}}(\cdot)} \mathcal{B}^P \xrightarrow{\Psi_{\text{PCA}}(\cdot)} \mathcal{B}_l^P. \quad (8)$$

where the operation “ $+\lambda_P \eta_i$ ” stands for the generation of PCF, the yielded $\mathcal{B}_l^P = \{\gamma_t^{\text{ref}} \in \mathbb{R}^{d_l} \mid \forall t = 1, \dots, T\}$. Then for the i -th ($i \in [1, 2, \dots, h_f \cdot w_f]$) test patch, the patch matching can be performed faster in this lower-dimensional space as

$$t^* = \arg \min_{\forall t=1, \dots, T} \|\gamma_i^{\text{tst}} - \gamma_t^{\text{ref}}\|_{l_2}, \quad (9)$$

where $\gamma_i^{\text{tst}} = \Psi_{\text{PCA}}(\mathbf{p}_i^{\text{tst}})$ represents the lower-dimensional PCF of the test patch.

4) *Matching with Similar Reference Images*: Secondly, to further increase the matching speed, we propose to *match a test patch only with the reference patches which belong to the “similar” reference images*. To define the image similarity, let us generate the image feature of an image I as

$$\begin{aligned} \mathbf{F} \in \mathbb{R}^{h_f \times w_f \times d_f} &\xrightarrow{+\lambda_P \eta} \mathbf{P} \in \mathbb{R}^{h_f \times w_f \times d_f} \\ &\downarrow \Psi_{\text{PCA}}(\cdot) \\ \mathbf{I} \in \mathbb{R}^{h_f \times w_f \times d_l} &\xleftarrow{\text{resize}} \mathbf{P}_l \in \mathbb{R}^{h_f \times w_f \times d_l}, \end{aligned} \quad (10)$$

where $\mathbf{F} = \Psi_{\text{CNN}}(I)$ as defined in Eq. 1, \mathbf{P} denotes the feature tensor containing $h_f \cdot w_f$ PCFs, the “resize” operation indicates to reduce the width and height of the feature tensor via interpolation. Then the distance between the j -th ($j \in [1, 2, \dots, N_{\text{trn}}]$) reference image I_j^{ref} and the test image I^{tst} writes

$$\delta_j = \Delta(I^{\text{tst}}, I_j^{\text{ref}}), \quad (11)$$

where $\Delta(\cdot)$ denotes the “robust distance” function which consider the image distance as a summation of patch-pair distances and ignores some of the most distant patch-pairs. Given all the distances between I^{tst} and the reference images storing in $\{\delta_1, \delta_2, \dots, \delta_{N_{\text{trn}}}\}$, the image indexes of I^{tst} ’s “similar reference images” are defined as

$$\{\delta_1, \delta_2, \dots, \delta_{N_{\text{trn}}}\} \xrightarrow{K\text{-NN Indexes}} \mathcal{Q} = \{q_1, q_2, \dots, q_K\} \quad (12)$$

5) *The Generation of PosFAR*: Given a test image I^{tst} and a set of defect-free training images $\{I_1^{\text{ref}}, I_2^{\text{ref}}, \dots, I_{N_{\text{trn}}}^{\text{ref}}\}$, one can firstly generate the ordinary bank $\mathcal{B}^P = \{\mathbf{p}_t^{\text{ref}} \in \mathbb{R}^{d_f} \mid \forall t = 1, \dots, T\}$ and the corresponding low-dimensional bank $\mathcal{B}_l^P = \{\gamma_t^{\text{ref}} \in \mathbb{R}^{d_l} \mid \forall t = 1, \dots, T\}$ as shown in Eq. 8. Meanwhile, the training image index of each element in \mathcal{B}^P are saved in the set $\{j_1, j_2, \dots, j_T\}$. The proposed faster patch matching then can be defined as

$$t^* = \arg \min_{\forall j_t \in \mathcal{Q}} \|\gamma_i^{\text{tst}} - \gamma_t^{\text{ref}}\|_{l_2}, \quad \forall i = 1, \dots, M, \quad (13)$$

where \mathcal{Q} denotes the K -NN indexes of I^{tst} as defined in Eq. 12, γ_i^{tst} stands for the lower-dimensional PCF feature of i -th patch in I^{tst} .

Finally, the PosFAR feature of each test patch is calculated as

$$\mathbf{r}_i = [\text{ABS}(\mathbf{p}_i^{\text{tst}} - \mathbf{p}_{t^*}^{\text{ref}})]^\theta \in \mathbb{R}^{d_f}, \quad \forall i, \quad (14)$$

where $\text{ABS}(\cdot)$ denotes the function of absolute value, $[\cdot]^\theta$ stands for the element-wise θ -power operation which is introduced to emphasize the larger elements in the residual vector. Compared with the distance-based residuals [18]–[21], PosFAR stores much richer intermedia information of patch matching. Further, each \mathbf{r}_i represents an “image block” which will be recognized as defective or defect-free by using the swin transformer model introduced below.

C. Train the Residual-based Swin Transformer for Block-wise Anomaly Detection

1) *Block-wise Anomaly Labels*: Encouraged by the successful pioneering work [18], [32], [36], [51], in this paper, a discriminative model is also employed to predict the anomaly score map for test images. In the conventional “unsupervised” setting (as described in Sec. II-A), pseudo defective regions are usually augmented and so that the segmentation model [18], [32], [36], [51] can be trained smoothly with the pixel-wise labels. However, considering that the PosFAR feature introduced above is block-wise, we thus propose to cast the original pixel-wise segmentation task into a block classification problem. Accordingly, the conventional pixel labels need to be converted into the block-wise ones.

Suppose that the pixel label map of an image $I \in \mathbb{R}^{h_I \times w_I \times 3}$ is denoted as $\mathbf{Y}_I^* \in \mathbb{R}^{h_I \times w_I}$, with -1 indicating defect-free pixels while 1 standing for the anomalous ones. We then can define our block-wise label map $\mathbf{Y}_f^* \in \mathbb{R}^{h_f \times w_f}$ as

$$\mathbf{Y}_f^*(r_f, c_f) = \begin{cases} 1 & \sum_{(r_1, c_1) \in \mathcal{U}_{r_f, c_f}} \mathbf{Y}_I^*(r_1, c_1) > \epsilon^+ \rho^2 \\ -1 & \sum_{(r_1, c_1) \in \mathcal{U}_{r_f, c_f}} \mathbf{Y}_I^*(r_1, c_1) < \epsilon^- \rho^2 \\ \emptyset & \text{otherwise} \end{cases} \quad (15)$$

where \mathcal{U}_{r_f, c_f} denotes the pixels belonging to the image block at coordinate $[r_f, c_f]$; $\rho = h_I/h_f = w_I/w_f$; ϵ^+ and ϵ^- are the two predefined thresholds; when labeled as \emptyset , the block is ignored during training, as introduced in Sec. III-C2. Fig. 3 illustrates this block labeling scheme.

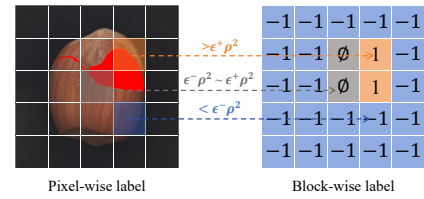


Fig. 3. The block labeling strategy employed in this work. The blocks with more than $\epsilon^+ \rho^2$ anomaly pixels are labeled 1 (red) while those blocks with less than $\epsilon^- \rho^2$ are labeled 0 (blue). The remaining blocks are labeled \emptyset and will be ignored in the training phase.

In this work, the block-wise labels are employed for the synthetic defects in the “unsupervised” setting as well as the

genuine defects in the “supervised” setting. The experimental results of this work verify the superiority of this labeling strategy. On the other hand, in real-life AD tasks, one only needs to manually label image blocks rather than pixels and thus significant reduction on annotation cost is achieved.

2) *Swin Transformer with Focal Loss*: We convert the AD task into a block-wise binary classification problem and solve it by using a Swin Transformer model [42]. In specific, given a test image $I^{1st} \in \mathbb{R}^{h_1 \times w_1 \times 3}$, its PosFARs $\mathbf{r}_i \in \mathbb{R}^{d_f}, \forall i$ are calculated via Equations 14 then fed into the Swin Transformer model as the input tokens [42], [55].

To suit the relatively small training sets in most anomaly detection challenges [9], [10], we design our Swin Transformer model with low complexity. As shown in Fig. 2, a linear embedding layer is firstly applied to the PosFAR features, projecting them into a 1024-dimensional space. Subsequently, 4 Swin Transformer blocks are employed to realize a 32-head self-attention within 8×8 regular windows (W-MSA) and shifted windows (SW-MSA). Finally, the tokens with each representing an image block are classified as normal or anomalous via a fully connected layer. In mathematics, we have

$$p_+^i = \Psi_{\text{Swin}}(\mathbf{r}_i), \forall i \in [1, 2, \dots, M], \quad (16)$$

where $p_+^i \in [0, 1]$ denotes the normalized anomaly confidence (of the i -th token) predicted by the Swin Transformer model $\Psi_{\text{Swin}}(\cdot)$

Considering that the normal image blocks usually dominate the original data distribution, we employ the focal loss [80] to lift the importance of the anomaly class. The focal loss used in this work writes:

$$\begin{aligned} \mathcal{L}_F = -\frac{1}{|\mathcal{Z}^-|} \sum_{i \in \mathcal{Z}^-} & \left[(1 - \alpha) p_+^i \gamma \log(1 - p_+^i) \right] \\ & - \frac{1}{|\mathcal{Z}^+|} \sum_{i \in \mathcal{Z}^+} \left[\alpha (1 - p_+^i) \gamma \log(p_+^i) \right] \end{aligned} \quad (17)$$

where \mathcal{Z}^+ and \mathcal{Z}^- stands for the training sample sets (here are transformer tokens) corresponding to defective (+) and defect-free (-) classes respectively.

3) *Randomly Masked Residuals*: Different from the vanilla vision transformers [42], [55], [56], the input to our model is essentially *feature residual vectors*. Most conventional data augmentation methods [74], [81], [82] designed for images can not be directly used in the current situation. By contrast, inspired by the recently proposed MAE algorithm [79], we design a simple but effective feature augmentation approach termed “Randomly Masked Residuals” for achieving higher generalization capacity. In specific, when training, each tokens $\{\mathbf{r}_1, \mathbf{r}_2, \dots, \mathbf{r}_M\}$ defined in Eq. 14 is randomly “masked” or “noised” as

$$\forall i, \mathbf{r}_i = \begin{cases} \mathbf{0}^T \in \mathbb{R}^{d_t} & \tau \in [0, \alpha] \\ \mathbf{r}_i + \kappa \frac{\|\mathbf{r}_i\|_{l_2}}{\|\mathbf{g}\|_{l_2}} \mathbf{g} & \tau \in (\alpha, 1] \end{cases} \quad (18)$$

where τ is a random variable sampled from the uniform distribution $[0, 1]$; α is the constant controlling the frequency of the reset operation; $\mathbf{g} \in \mathbb{R}^{d_f}$ denotes a Gaussian noise vector; $\kappa \in [0, 1]$ is a small constant for residual jittering.

We found this augmentation approach can effectively increase the final performance of the proposed method, as shown in Sec. IV-F.

4) *Off-the-shelf methods for generating fake anomalies*: In the “unsupervised” setting of AD tasks, one needs to generate fake anomalies to train a discriminative model properly. In this work, we follow the off-the-shelf fake/simulated anomaly generation approach proposed in the MemSeg algorithm [51]. Readers are recommended to the original work [51] for more details. Note that we also employ this anomaly generation method for the supervised and weakly-supervised settings to increase the variation of the training samples.

5) *Inference of the swin transformer*: Given $\{p_+^1, p_+^2, \dots, p_+^M\}$ standing for the anomaly confidences of image blocks predicted by the Swin Transformer model $\Psi_{\text{Swin}}(\cdot)$, one can obtain the image-size anomaly map $\mathbf{P}_+^* \in \mathbb{R}^{h_f \times w_f}$ as

$$\{p_+^1, \dots, p_+^M\} \xrightarrow{\text{reshape}} \mathbf{P}_+ \in \mathbb{R}^{h_f \times w_f} \xrightarrow{\text{upsample}} \mathbf{P}_+^* \quad (19)$$

D. Exploiting the Unlabeled Information via ResMixMatch

1) *The Weaker Labels with Trivial Labeling Cost*: To further reduce the annotation cost, we introduce three types of anomaly labels which are even “cheaper” than the block-wise ones. As depicted in Fig. 4, the proposed weak labels include the “rotated bounding-boxes” (left), the “axis-aligned bounding-boxes” (middle) and the “image-level labels” (right). From the figure we can see that the bounding box labels are the minimal rectangles covering the whole defective region, with or without rotation. On the other hand, the image-level label just represents the defective status of the image. These weak labels only requires the annotators input a few (1 to 4) clicks on the image.

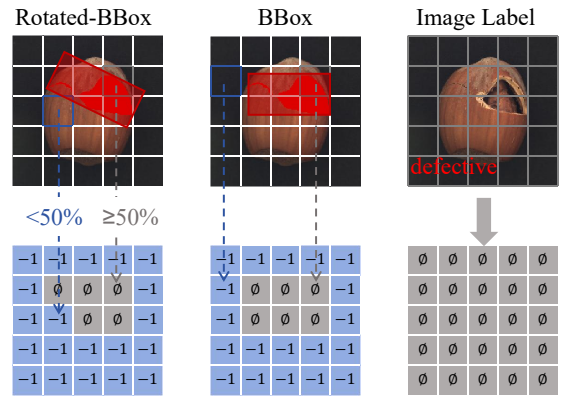


Fig. 4. The three types of weak labels employed in this work. From left to right: the “rotated bounding-boxes” (left), the “axis-aligned bounding-boxes” (middle) and the “image-level labels” (right). The lower part of each column illustrates the block-wise label converting operation for the associated weak label

In the block-based framework of this work, one needs to convert the weaker labels into the block-wise annotations for model training. The lower part of Fig. 4 illustrates the label converting processes for the three kinds of weak labels. In a nutshell, for the bounding-box-based labels, we consider the outside blocks (overlapping ratio greater than 50%) of the bounding boxes as normal while the inside blocks (overlapping

ratio less than 50%) are treated as “unknown”. In contrast, all the blocks of a image labeled as defective are unknown.

Note that the proposed weak labels are partially inspired by the pioneering works [38], [41] that also employ bounding boxes to annotate defective parts. However, our labeling strategy is less misleading and the unknown region can be successfully exploited by the semi-supervised learning scheme introduced below.

2) Exploiting the Unlabeled blocks in a Semi-Supervised Manner: The proposed weaker labels can achieve very efficient annotation processes. However, they arise another difficulty in training: An unignorable portion of the image blocks are unlabeled and no block is labeled as “defective”.

Fortunately, this semi-supervised situation is highly well studied in the machine learning literature [43], [68]–[71]. In this work, we borrow the high-level concept of the MixMatch method [43] into the learning process of a Swin Transformer model. The novel semi-supervised learning algorithm, termed “ResMixMatch”, is summarized in Algorithm 1.

From the algorithm we can see that, different from MixMatch [43] that treats every sample independently, in ResMixMatch, all the PosFAR features are related. The Swin Transformer model can effectively link the PosFARs from the same image via the self-attention mechanism and their anomaly confidences are then predicted depending on each other. The labels of the “unknown” blocks are estimated not only by the mixing-matching strategy but also based on the neighboring information. In this way, the “label guessing” becomes more confident.

E. Foreground Region Estimation based on Coreset Sampling

Recent researches on industrial anomaly detection [37], [51], [83] illustrates the performance gain by focusing on the foreground area in the object-oriented tasks. In this paper, we also follow this methodology to reduce the anomaly scores of uninterested background areas. However, instead of conducting the traditional image binarization, this work estimates the object region in a novel and more effective way.

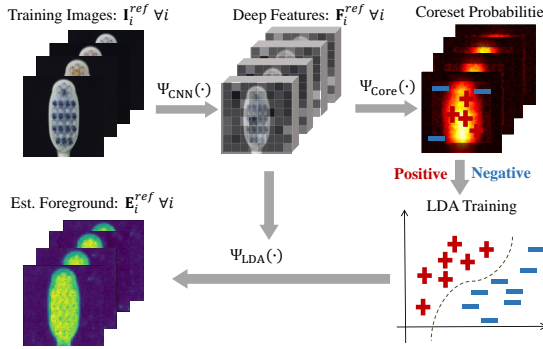


Fig. 5. The training and inference process of the coreset-based foreground estimation method proposed in this work. Note that as a prior constraint, the sampling ratio of positive (foreground) samples in the image boundaries are reduced.

In practice, we observe that the “coreset” algorithm (Eq. 3) employed in PatchCore [18] and inherited by this paper samples the foreground patches much more frequently than the

Algorithm 1 ResMixMatch training of WeakREST

- 1: **Input:** Swin Transformer model $\Psi_{\text{Swin}}(\cdot)$, PosFARs $\mathbf{r}_i \in \mathbb{R}^{d_f}$, the corresponding labels $y_i^* \in \{-1, \emptyset(\text{unknown})\}$, $i = 1, 2, \dots, M$, sharpening temperature t , unlabeled loss weight λ_u , number of augmentations A , and focal loss parameters $\{\alpha_x, \alpha_u, \gamma_x, \gamma_u\}$.
- 2: **A-Augmentation** as Equation 18
 $\forall i, \{\mathbf{r}_{i,j}, \forall j | j = 1, 2, \dots, A\} \leftarrow A\text{-Augmentation} \leftarrow \mathbf{r}_i$
 $\forall i, \{y_{i,j}^*, \forall j | j = 1, 2, \dots, A\} \leftarrow \text{Copy} \leftarrow y_i^*$,
- 3: **Guess pseudo labels through augmentation** [43]
 $\forall i, \{\bar{y}_{i,j}, \forall j | j = 1, 2, \dots, A\} \leftarrow \text{Copy}$
 $\leftarrow \text{Sharpen} \left(\frac{1}{A} \sum_{j=1}^A \Psi_{\text{Swin}}(\mathbf{r}_{i,j}), t \right)$
- 4: **Divide the tokens into labeled set \mathcal{X} and unlabeled set \mathcal{U}** [43]
 $\mathcal{X} = \{X_i = \{\mathbf{r}_i, y_i^*\}, \forall i | y_i^* = 0\}$
 $\mathcal{U} = \{U_i = \{\mathbf{r}_i, \bar{y}_i\}, \forall i | y_i^* = -1\}$
- 5: **Combine the labeled and unlabeled tokens and shuffle**
 $\mathcal{W} = \text{Shuffle}(\text{Union}(\mathcal{X}, \mathcal{U}))$
- 6: **Apply MixUp to all tokens** [43]
 $\hat{\mathcal{X}} \leftarrow \{\text{MixUp}(X_i, W_i), \forall i | i = 1, \dots, |\mathcal{X}|\}$
 $\hat{\mathcal{U}} \leftarrow \{\text{MixUp}(U_i, W_{i+|\mathcal{X}|}), \forall i | i = 1, \dots, |\mathcal{U}|\}$
- 7: **Randomly mask tokens as Equation 18**
 $\forall \{\hat{\mathbf{r}}_i, \hat{y}_i\} \in \text{Union}(\mathcal{X}, \mathcal{U}), \{\hat{\mathbf{r}}_i, \hat{y}_i\} = \text{RandomMask}(\hat{\mathbf{r}}_i, \hat{y}_i)$
- 8: **Classify the tokens**
 $\forall i, \hat{p}_+^i = \Psi_{\text{Swin}}(\hat{\mathbf{r}}_i)$
- 9: **Compute the labeled loss \mathcal{L}_x and unlabeled loss \mathcal{L}_u**
 $\mathcal{Z}_k^+ = \{\forall i | y_i^* = -1 \& \hat{y}_i > 0.5\}$
 $\mathcal{Z}_u^+ = \{\forall i | y_i^* = \emptyset \& \hat{y}_i > 0.5\}$
 $\mathcal{Z}_k^- = \{\forall i | y_i^* = -1 \& \hat{y}_i \leq 0.5\}$
 $\mathcal{Z}_u^- = \{\forall i | y_i^* = \emptyset \& \hat{y}_i \leq 0.5\}$
 $\mathcal{L}_x = -\frac{1}{|\mathcal{Z}_k^-|} \sum_{i \in \mathcal{Z}_k^-} \left[(1 - \alpha_x) \hat{p}_+^i \gamma_x \log(1 - \hat{p}_+^i) \right]$
 $\quad - \frac{1}{|\mathcal{Z}_k^+|} \sum_{i \in \mathcal{Z}_k^+} \left[\alpha_x (1 - \hat{p}_+^i) \gamma_x \log(\hat{p}_+^i) \right]$
 $\mathcal{L}_u = -\frac{1}{|\mathcal{Z}_u^-|} \sum_{i \in \mathcal{Z}_u^-} \left[(1 - \alpha_u) \hat{p}_+^i \gamma_u \log(1 - \hat{p}_+^i) \right]$
 $\quad - \frac{1}{|\mathcal{Z}_u^+|} \sum_{i \in \mathcal{Z}_u^+} \left[\alpha_u (1 - \hat{p}_+^i) \gamma_u \log(\hat{p}_+^i) \right]$
- 10: **Output:** $\mathcal{L}_{\text{mix}} = \mathcal{L}_x + \lambda_u \mathcal{L}_u$

background ones (see Fig. 5). This phenomenon mainly stems from the coreset’s preference to the “representatives” patterns in the raw bank. Considering that background regions of AD images usually contains much less pattern variations than the foreground parts, coreset will thus pay more attention to the foreground of the image.

In this work, we propose to estimate the foreground region via binary classification. And the positive (foreground) training instances are sampled according to the sampling probability map of the coresnet algorithm while the negative ones (background) are sampled based on the complement probability. The learned LDA model $\Psi_{\text{LDA}}(\cdot)$ is fed with the CNN feature $\mathbf{F} \in \mathbb{R}^{h_f \times w_f}$ (Eq. 1) and calculate foreground confidence map as $\mathbf{E} = \Psi_{\text{LDA}}(\mathbf{F}) \in \mathbb{R}^{h_f \times w_f}$. Fig. 5 depicts the foreground estimation process for the training images.

Finally, for a test image \mathbf{I}^{tst} , we reweight its anomaly map $\mathbf{P}_+ \in \mathbb{R}^{h_f \times w_f}$ (Eq. 19) by the foreground information as

$$\tilde{\mathbf{P}}_+ = [\text{MaxPool}(\{\mathbf{E}_1^{\text{ref}}, \mathbf{E}_2^{\text{ref}}, \dots, \mathbf{E}_K^{\text{ref}}\})]^r \cdot \mathbf{P}_+, \quad (20)$$

where the set $\{\mathbf{E}_1^{\text{ref}}, \mathbf{E}_2^{\text{ref}}, \dots, \mathbf{E}_K^{\text{ref}}\}$ stores the estimated foreground maps of \mathbf{I}^{tst} 's K -NN reference image, as introduced in Eq. 12, parameter $r < 1$ is set to adjust the influence from the foreground estimation. In other words, we *do not directly infer the foreground region of the test image* as it might be broken due to the defect. In contrast, we *estimate the “rectified” foreground region of \mathbf{I}^{tst} with the “union” of the foreground regions of its neighboring reference images*. In the experiment of this paper, the proposed foreground estimation method illustrates its superiority, in terms of both speed and accuracy.

F. Implementation details

In this work, all images are resized to 512×512 , and a Wide-ResNet-50 model [84] (pre-trained on ImageNet-1K [53]) is employed as $\Psi_{\text{CNN}}(\cdot)$ to extract deep features. Feature maps from layers 1, 2, and 3 are combined to form $d_f = 1024$ feature vectors, as described in [18]. From these, 10% are sampled to build the bank \mathcal{B} . The parameters $\lambda_P = 0.03$ for texture categories and $\lambda_P = 0.15$ for object categories are set to generate PCFs. Residual features at $\theta = 1$ and $\theta = 2$ are concatenated and pooled to maintain the original dimension. Additionally, features from layer 1 of $\Psi_{\text{CNN}}(\cdot)$ are applied to attain $K = 64$ nearest images (see Eq. 12), while features from layer 2 are exploited to conduct foreground region estimation with $r = 0.15$ for object categories (see Eq. 20).

The Swin model is trained using the AdamW optimizer with a weight decay of 0.05, a learning rate of 5×10^{-5} , and an Exponential Moving Average (EMA) decay of 0.999. Models are trained from scratch in an unsupervised setting or with block labels. Unsupervised models are used to initialize weights with ResMixMatch 1, applying a sharpening temperature of $t = 0.5$ and linearly ramping up the unlabeled loss weight to $\lambda_u = 5$ over the first 400 steps of training, following the MixMatch algorithm [43]. The parameters of the focal loss $\alpha_x, \alpha_u, \gamma_x$, and γ_u are set to 0.25, 0.75, 4, and 4, respectively.

To compare the final prediction map with the ground-truth label map, it is first upscaled to the same size as the ground-truth via bilinear interpolation and then smoothed using a Gaussian kernel of 4, as done in [18].

IV. EXPERIMENTS

A. Experiment Setting

In this section, extensive experiments are carried out to evaluate the proposed method, compared with a comprehen-

sive collection of SOTA methods including DRAEM [50], RD [30], SSPCAB [85], DMAD [34], SimpleNet [86], DeSTSeg [32], PyramidFlow [47], CFLOW [78], RD++ [87], PRN [36], BGAD [37], DevNet [88], DRA [35], RealNet [83] and AHL [89]. Considering the conceptual similarity in methodology, we also involve a SOTA method of weakly supervised segmentation, *i.e.* BoxTeacher [90], in the comparison to illustrate the practical advantage of WeakREST. The comparison is conducted on three well-acknowledged benchmarks, namely, the MVTec-AD [9] dataset, the BTAD [10] dataset and the KolektorSDD2 dataset [41], respectively. The involved AD algorithms are measured comprehensively by four popular threshold-independent metrics: Image-AUROC, Pixel-AUROC, PRO [91] (Per Region Overlap) and AP [50] (Average Precision). The first one focus on the precision of image-level anomaly detection while the latter three measure the performance of anomaly localization.

We perform all the experiments in both the unsupervised and supervised settings. In the unsupervised scenario, only normal data can be accessed during training but synthetic defects are artificially generated with pixel-wise labels. As to the supervised AD tasks, we randomly draw 10 anomalous images with various types of defects to the train set and remove them from the test set. This operation strictly follows the data splitting principle in [36] and [35]. In supervised experiments, the WeakREST model is firstly pretrained in the unsupervised condition and then fine-tuned using the genuine defective samples. The required block-wise labels of our methods are converted by using the method introduced in Sec. III-C1 (for pixel labels) and Sec. III-D1 (for bounding-box and image-level labels). All the experiments are conducted on a PC with a Intel i5-13450 CPU, 64G RAM and an NVIDIA RTX4090 GPU.

B. Results on MVTec-AD

MVTec-AD [9] is the most popular AD dataset with 5,354 high-resolution color images belonging to 5 texture categories and 10 object categories. Each category contains a training set with only normal images and a test set with various kinds of defects as well as defect-free images. We conduct the experiments on this dataset within both unsupervised and supervised conditions.

The unsupervised AD results of the comparing algorithms on MVTec-AD [9] are shown in Table I. As shown in the table, our method achieves the highest average AP, average PRO and average pixel AUROC for both texture and object categories and outperforms the unsupervised SOTA by 7.2%, 1.7% and 0.4% respectively. Specifically, WeakREST ranks first on 93% (14 out of 15) categories with AP metric and the “first-ranking” ratios for the PRO and Pixel-AUROC are 53% and 67%. As to image-level metric image-AUROC, our method also achieves the highest accuracy (99.6%) which evens the performances of SimpleNet [86] and RealNet [83].

In addition, Table II illustrates that, trained with genuine defective samples, the WeakREST model still ranks first for the average AD performance evaluated by using all three metrics. In particular, our method outperforms the supervised SOTAs

Method	PatchCore [18] (CVPR2022)	DRAEM [50] (ICCV2021)	NFAD [37] (CVPR2023)	DMAD [34] (CVPR2023)	SimpleNet [86] (CVPR2023)	DeSTSeg [32] (CVPR2023)	PyramidFlow [47] (CVPR2023)	RD++ [87] (CVPR2023)	RealNet [83] (CVPR2024)	Ours
Carpet	64.1/95.1/99.1	53.5/92.9/95.5	74.1/98.2/99.4	63.8/95.9/99.0	44.1/92.0/97.7	72.8/~/96.1	~/97.2/97.4	~/97.7/99.2	62.1/96.1/98.9	81.6/98.3/99.4
Grid	30.9/93.6/98.8	65.7/98.3/99.7	51.9/97.9/99.3	47.0/97.3/99.2	39.6/94.6/98.7	61.5/~/99.1	~/94.3/95.7	~/97.7/99.3	59.2/96.9/99.5	74.6/98.7/99.7
Leather	45.9/97.2/99.3	75.3/97.4/98.6	70.1/99.4/99.7	53.1/98.0/99.4	48.0/97.5/99.2	75.6/~/99.7	~/99.2/98.7	~/99.2/99.4	72.6/93.0/99.7	79.9/99.5/99.8
Tile	54.9/80.2/95.7	92.3/98.2/99.2	63.0/91.8/96.7	56.5/84.3/95.8	63.5/78.3/93.9	90.0/~/98.0	~/97.2/97.1	~/92.4/96.6	92.2/93.7/99.1	95.4/98.7/99.6
Wood	50.0/88.3/95.0	77.7/90.3/96.4	62.9/95.6/96.9	45.5/89.3/94.8	48.8/83.9/93.9	81.9/~/97.7	~/97.9/97.0	~/93.3/95.8	77.3/91.0/98.4	84.7/97.1/98.2
Average	49.2/90.9/97.6	72.9/95.4/97.9	64.4/96.6/98.4	53.2/93.0/97.6	48.8/89.3/96.7	76.4/~/98.1	~/97.2/97.2	~/96.1/98.1	72.7/94.1/99.1	83.2/98.5/99.3
Bottle	77.7/94.7/98.5	86.5/96.8/99.1	77.9/96.6/98.9	79.6/96.4/98.8	73.0/91.5/98.0	90.3/~/99.2	~/95.5/97.8	~/97.0/98.8	86.8/ 97.2/99.2	93.6/97.8/99.5
Cable	66.3/93.2/ 98.4	52.4/81.0/94.7	65.7/ 95.9/98.0	58.9/92.2/97.9	69.3/89.7/97.5	60.4/~/97.3	~/90.3/91.8	~/93.9/ 98.4	54.3/91.1/97.6	84.1/95.5/99.3
Capsule	44.7/94.8/99.0	49.4/82.7/94.3	58.7/96.0/ 99.2	42.2/91.6/98.1	44.7/92.8/98.9	56.3/~/99.1	~/98.3/98.6	~/96.4/ 98.8	59.1/90.5/99.3	63.7/96.3/99.2
Hazelnut	53.5/95.2/98.7	92.9/98.5/99.7	65.3/97.6/98.6	63.4/95.9/99.1	48.3/92.2/97.6	88.4/~/99.6	~/98.1/98.1	~/96.3/99.2	80.5/92.9/99.5	85.5/ 98.2/99.5
Metal nut	86.9/94.0/98.3	96.3/97.0/99.5	76.6/94.9/97.7	79.0/94.2/97.1	92.6/91.3/98.7	93.5/~/98.6	~/91.4/97.2	~/93.0/98.1	82.1/95.1/98.1	98.3/98.1/99.8
Pill	77.9/95.0/97.8	48.5/88.4/97.6	72.6/98.1/98.0	79.7/96.9/98.5	80.1/93.9/98.5	83.1/~/98.7	~/96.1/96.1	~/97.0/98.3	80.7/90.0/ 99.0	84.6/96.7/99.0
Screw	36.1/97.1/ 99.5	58.2/95.0/97.6	47.4/96.3/99.2	47.9/96.5/99.3	38.8/95.2/99.2	58.7/~/98.5	~/94.7/94.6	~/98.6/ 99.7	49.2/94.0/99.4	67.1/97.3/99.5
Toothbrush	38.3/89.4/98.6	44.7/85.6/98.1	38.8/92.3/98.7	71.4/91.5/ 99.3	51.7/88.7/98.6	75.2/~/99.3	~/97.9/98.5	~/94.2/99.1	51.3/90.7/98.7	80.8/97.2/99.7
Transistor	66.4/92.4/96.3	50.7/70.4/90.9	56.0/82.0/94.0	58.5/85.2/94.1	69.0/93.2/96.8	64.8/~/89.1	~/94.7/96.9	~/81.8/94.3	69.1/94.1/97.6	82.5/95.3/97.2
Zipper	62.8/95.8/98.9	81.5/ 96.8/98.8	56.0/95.7/98.6	50.1/93.8/97.9	60.0/91.2/97.8	85.2/~/99.1	~/95.4/96.6	~/96.3/98.8	64.6/95.0/98.9	89.1/98.7/99.7
Average	61.1/94.2/98.4	66.1/89.2/97.0	61.5/94.5/98.1	63.1/93.4/98.0	62.7/92.0/98.2	75.6/~/97.9	~/95.2/96.6	~/94.5/98.4	67.8/93.1/ 98.7	82.9/97.1/99.2
Total Average	57.1/93.1/98.1	68.4/91.3/97.3	62.5/95.2/98.2	59.8/93.3/97.9	58.1/91.1/97.7	75.8/~/97.9	~/95.9/96.8	~/95.0/98.3	69.4/93.4/ 98.9	83.0/97.6/99.3
Image AUROC	99.1	98.0	97.4	99.5	99.6	98.6	~	99.4	99.6	99.6

TABLE I

THE COMPARISON OF THE AVERAGE PRECISION (AP), PER-REGION OVERLAP (PRO), PIXEL AUROC AND IMAGE AUROC METRICS UNDER UNSUPERVISED SETTING ON THE MVTec-AD DATASET. THE BEST ACCURACY IN ONE COMPARISON WITH THE SAME DATA AND METRIC CONDITION IS SHOWN IN RED WHILE THE SECOND ONE IS SHOWN IN BLUE.

Method	PRN [36] (CVPR2023)	BGAD [37] (CVPR2023)	DevNet [88] (arXiv2021)	BoxTeacher [90] (CVPR2023)	DRA [35] (CVPR2022)	AHL [89] (CVPR2024)	Ours			
	Pixel	Pixel	Pixel	BBox	Image	Image	Block	Rbbox	BBox	Image
Carpet	82.0/97.0/99.0	83.2/98.9/99.6	45.7/85.8/97.2	78.3/96.4/99.2	52.3/92.2/98.2	~/~/~/	88.4/99.1/99.7	88.6/99.1/99.8	87.9/ 99.1/99.7	82.9/98.6/99.5
Grid	45.7/95.9/98.4	59.2/98.7/98.4	25.5/79.8/87.9	60.0/97.9/99.4	26.8/71.5/86.0	~/~/~/	76.7/98.7/99.7	75.6/98.8/99.8	74.0/ 98.7/99.7	75.1/98.6/ 99.7
Leather	69.7/99.2/99.7	75.5/99.5/99.8	8.1/88.5/94.2	56.2/97.3/98.6	5.6/84.0/93.8	~/~/~/	85.7/99.6/99.9	84.1/99.6/99.9	83.9/ 99.7/99.9	76.9/95.5/99.8
Tile	96.5/98.2/99.6	94.0/97.9/99.3	52.3/78.9/92.7	91.7/96.8/98.7	57.6/81.5/92.3	~/~/~/	97.4/99.2/99.8	97.7/99.2/99.8	97.6/99.2/99.8	96.9/99.1/99.7
Wood	82.6/95.9/97.8	78.7/96.8/98.0	25.1/75.4/86.4	67.4/93.4/96.2	22.7/69.7/82.9	~/~/~/	90.7/98.5/99.3	90.8/98.6/99.3	90.2/98.4/99.2	86.2/97.6/98.4
Average	75.3/97.2/98.9	78.1/98.4/99.2	31.3/81.7/91.7	70.7/96.4/98.4	33.0/79.8/90.6	~/~/~/	87.8/99.0/99.7	87.3/99.1/99.7	86.7/ 99.0/99.7	84.1/98.7/99.4
Bottle	92.3/97.0/99.4	87.1/97.1/99.3	51.5/83.5/93.9	82.7/92.0/97.2	41.2/77.6/91.3	~/~/~/	93.6/98.3/99.6	93.2/97.9/ 99.7	92.8/97.7/ 99.6	93.8/98.1/99.6
Cable	78.9/ 97.2/98.8	81.4/ 97.7/98.5	36.0/80.9/88.8	64.5/81.2/85.3	34.7/77.7/86.6	~/~/~/	88.8/96.0/99.4	87.6/96.8/99.5	87.1/96.5/ 99.5	84.5/95.5/99.3
Capsule	62.2/92.5/98.5	58.3/96.8/98.8	15.5/83.6/91.8	48.1/83.1/91.3	11.7/79.1/89.3	~/~/~/	71.3/97.5/99.5	71.6/98.2/99.5	68.7/ 97.9/99.4	66.8/97.2/99.4
Hazelnut	93.8/97.4/99.7	82.4/98.6/99.4	22.1/83.6/91.1	77.4/95.4/99.5	22.5/86.9/89.6	~/~/~/	86.9/ 98.8/99.7	86.7/99.0/99.6	86.3/ 98.8/99.6	88.1/98.5/99.6
Metal nut	98.0/95.8/99.7	97.3/96.8/99.6	35.6/76.9/77.8	88.6/79.2/97.4	29.9/76.7/77.9	~/~/~/	93.9/98.2/99.9	98.9/98.3/99.9	98.8/ 98.4/99.9	98.6/ 98.3/99.8
Pill	91.3/97.2/99.5	92.1/98.7/99.5	14.6/69.2/82.6	75.2/85.8/96.4	21.6/77.0/84.5	~/~/~/	93.4/97.8/99.7	94.8/98.7/99.8	93.9/97.7/99.7	88.7/97.3/99.5
Screw	44.9/92.4/97.5	55.3/96.8/99.3	1.4/31.1/60.3	35.3/56.8/79.6	5.0/30.1/54.0	~/~/~/	71.8/98.1/99.7	71.5/98.2/99.7	70.9/97.9/ 99.7	70.0/97.7/99.6
Toothbrush	78.1/95.6/99.6	71.3/96.4/99.5	6.7/33.5/84.6	41.0/72.5/94.6	4.5/56.1/75.5	~/~/~/	84.8/ 98.0/99.7	85.4/97.5/ 99.7	85.6/97.5/99.7	85.5/97.6/99.7
Transistor	85.6/94.8/98.4	82.3/97.1/97.9	6.4/39.1/56.0	32.1/52.8/70.8	11.0/49.0/79.1	~/~/~/	94.0/99.0/99.6	88.5/98.7/99.2	87.0/98.5/99.0	83.5/97.1/98.2
Zipper	77.6/95.5/98.8	78.2/97.7/99.3	19.6/81.3/93.7	73.9/96.8/99.0	42.9/91.0/96.9	~/~/~/	91.5/99.1/99.8	90.4/98.9/99.7	90.4/98.9/99.7	89.2/98.7/ 99.7
Average	80.3/95.5/99.0	78.6/97.4/99.1	20.9/66.3/82.1	61.9/79.6/91.1	22.5/70.1/82.6	~/~/~/	87.5/98.1/99.6	87.0/98.2/99.6	86.1/98.0/ 99.6	84.8/97.6/99.4
Total Average	78.6/96.1/99.0	78.4/97.7/99.2	24.4/71.4/85.3	64.8/85.2/93.5	26.0/73.3/85.3	~/~/~/	87.6/98.4/99.7	87.1/98.5/99.7	86.3/98.3/99.6	84.6/98.0/99.4
Image AUROC	99.4	99.3	94.5	83.4	95.9	97.0	99.8	99.8	99.8	99.7

TABLE II

THE COMPARISON OF THE AVERAGE PRECISION (AP), PER-REGION OVERLAP (PRO), PIXEL AUROC AND IMAGE AUROC METRICS FOR SUPERVISED AD ON THE MVTec-AD DATASET. THE BEST ACCURACY IN ONE COMPARISON WITH THE SAME DATA AND METRIC CONDITION IS SHOWN IN RED WHILE THE SECOND ONE IS SHOWN IN BLUE.

by 9.0% on AP, 0.7% on PRO and 0.5% on Pixel-AUROC. The “first-ranking” ratios of WeakREST in the supervised scenario are 93%, 80% and 93% one AP, PRO and Pixel-AUROC respectively. Similar to the unsupervised scenario, the proposed method outperforms all the SOTA methods on Image-AUROC in the supervised setting. A new record of Image-AUROC 99.8% is obtained by WeakREST.

It is interesting to see that with only weak labels, WeakREST performances consistently better than the existing AD algorithm with full supervision. In particular, the WeakREST learned with image tags, which requires negligible annotation cost, beats all the SOTA methods with much more finer labels. The proposed algorithm illustrates remarkably high capacities of exploiting the information of unlabeled regions. Readers can also find the qualitative results of the proposed method compared with other SOTA algorithms in Figure 7.

C. Results on BTAD

As a more challenging alternative to MVTec-AD, BTAD [10] (beanTech Anomaly Detection) contains 2,830 high-resolution color images of three industrial products. Each product includes normal images in the train set and the corresponding test set consists of both defective and defect-free images.

We evaluate our algorithm on the BTAD dataset with those SOTA methods also reporting their results on this dataset. Table III shows that WeakREST achieves better performances to the unsupervised SOTA. The only exception occurs in the comparison on Image-AUROC where our method ranks the third (slightly worse than RealNet [83] and PyramidFlow [47]). Furthermore, as shown in Table IV, in the supervised condition, the proposed method surpasses SOTA methods by large margins: 9.7%, 4.5%, 0.6% and 1.8% on AP, PRO, Pixel-AUROC and Image-AUROC, respectively. Similar to the

Method	PatchCore [18] (CVPR2022)	DRAEM [50] (ICCV2021)	SSPCAB [85] (CVPR2022)	CFLOW [78] (WACV2022)	RD [30] (CVPR2022)	PyramidFlow [47] (CVPR2023)	NFAD [37] (CVPR2023)	RD++ [87] (CVPR2023)	RealNet [83] (CVPR2024)	Ours
01	47.1/78.4/96.5	17.0/61.4/91.5	18.1/62.8/92.4	39.6/60.1/94.8	49.3/72.8/95.7	~/~/97.4	46.7/76.6/96.7	~/73.2/96.2	67.0/83.5/98.4	66.8/85.7/98.4
02	56.3/54.0/94.9	23.3/39.0/73.4	15.8/28.6/65.6	65.5/56.9/93.9	66.1/55.8/96.0	~/~/97.6	59.2/57.9/96.4	~/71.3/96.4	54.3/49.1/95.9	83.8/70.5/98.0
03	51.2/96.4/99.2	17.2/84.3/96.3	5.0/71.0/92.4	56.8/97.9/99.5	45.1/ 98.8/99.0	~/~/98.1	62.8/98.8/99.7	~/87.4/ 99.7	54.7/90.0/99.6	38.7/98.4/ 99.7
Average	51.5/76.3/96.9	19.2/61.6/87.1	13.0/54.1/83.5	54.0/71.6/96.1	53.5/75.8/96.9	~/~/97.7	56.2/ 77.8/97.6	~/77.3/97.4	58.7/74.2/98.0	63.1/84.9/98.7
Image AUROC	92.6	89.0	88.3	90.5	94.3	95.8	94.6	95.6	96.1	94.4

TABLE III

RESULTS OF THE AP, PRO, PIXEL AUROC AND IMAGE AUROC METRICS UNDER UNSUPERVISED SETTING ON BTAD. THE BEST ACCURACY IN ONE COMPARISON WITH THE SAME DATA AND METRIC CONDITION IS SHOWN IN RED WHILE THE SECOND ONE IS SHOWN IN BLUE.

Method	PRN [36] (CVPR2023)	BGAD [37] (CVPR2023)	BoxTeacher [90] (CVPR2023)	Ours				
	Supervision	Pixel	Pixel	BBox	Block	Rbbox	BBox	Image
01	64.0/86.6/98.4	38.8/81.4/96.6	59.0/ 92.2 /98.6	84.7/94.0/99.4	79.0/89.8/99.1	78.6/88.8/98.9	59.8/85.5/98.4	
02	83.4/66.5/97.9	65.7/54.4/95.1	59.3/ 80.3 /96.4	87.8/78.9/98.5	85.7/74.1/98.3	84.8/73.4/98.2	82.9/69.6/97.9	
03	77.4/99.5/99.9	57.4/98.3/99.6	22.8/86.4/97.1	81.2/99.6/99.9	54.8/98.3/99.4	69.6/99.4/ 99.9	39.0/98.8/99.7	
Average	74.9/84.2/98.7	54.0/78.0/97.1	47.0/86.3/97.3	84.6/90.8/99.3	73.2/ 87.4/98.9	77.7/87.2/99.0	60.6/84.7/98.7	
Image AUROC	94.7	94.5	74.6	96.5	95.8	96.0	94.2	

TABLE IV

RESULTS OF THE AP, PRO AND PIXEL AUROC AND IMAGE AUROC METRICS FOR SUPERVISED AD PERFORMANCE ON BTAD. THE BEST ACCURACY IN ONE COMPARISON WITH THE SAME DATA AND METRIC CONDITION IS SHOWN IN RED WHILE THE SECOND ONE IS SHOWN IN BLUE.

situation of MVTec-AD, the weakly-supervised WeakREST models also obtains higher average performances than the fully-supervised SOTA algorithms.

D. Results on KolektorSDD2

KolektorSDD2 [41] dataset is designed for surface defect detection and includes various types of defects, such as scratches, minor spots, and surface imperfections. It comprises a training set with 246 positive (defective) and 2,085 negative (defect-free) images, as well as a test set with 110 positive and 894 negative images. We compare the performances of WeakREST with the SOTA results available in the literature.

As shown in Table V, the unsupervised WeakREST beats SOTA methods with a clear superiority (12.8%, 3.8%, 2.1% and 0.1% for AP, PRO, Pixel-AUROC and Image-AUROC, respectively). Under the supervised condition, our method also achieves better results and the WeakREST model supervised by image labels can already outperform existing methods with pixel-wise annotations.

E. Analysis on weak labels

Recall that the main motivation of this work is to reduce the labeling cost of AD tasks, we report the annotation time-consumption of the proposed two weak labels compared with pixel-level annotations.

To obtain the labeling time, the pixel labels, block labels, bounding boxes and the image tags of anomalies on a subset of MVTec-AD (10 defective images for each sub-category) are all manually annotated. Four master students majoring in computer vision complete the labeling task using the labeling tool proposed in this work.

The average annotation times of three kinds of labels are illustrated in Figure 6, along with the corresponding AD performances (Image-AUROC, Pixel-AUROC, PRO and AP). According to the figure, one requires only around 0.5 seconds to label an defective image. Besides, it takes around

Method	Supervision	AP	PRO	P-AUROC	I-AUROC
PatchCore [18]	Un	64.1	88.8	97.1	94.6
DRAEM [50]	Un	39.1	67.9	85.6	81.1
SSPCAB [85]	Un	44.5	66.1	86.2	83.4
CFLOW [78]	Un	46.0	93.8	97.4	95.2
RD [30]	Un	43.5	94.7	97.6	96.0
Ours	Un	76.9	98.5	99.7	96.1
PRN [36]	Pixel	72.5	94.9	97.6	96.4
Box2Mask [92]	BBox	35.3	74.8	79.2	86.1
BoxTeacher [90]	BBox	23.2	79.3	90.9	74.9
Ours	Block	77.7	99.0	99.7	97.9
Ours	Rbbox	76.9	98.9	99.7	97.5
Ours	BBox	76.4	98.8	99.7	97.6
Ours	Image	77.0	98.7	99.7	97.7

TABLE V

RESULTS OF ANOMALY LOCALIZATION PERFORMANCE ON KOLEKTORSDD2. THE BEST ACCURACY IN ONE COMPARISON WITH THE SAME DATA AND THE METRIC CONDITION IS SHOWN IN RED WHILE THE SECOND ONE IS SHOWN IN BLUE. NOTE THAT THE UPPER SUB-TABLE SHOWS THE RESULTS OBTAINED IN THE UNSUPERVISED CONDITION AND THE LOWER PART REPORTS THOSE WITH GENUINE DEFECTIVE SAMPLES.

ϵ^+	ϵ^-	Unsupervised	Weak-sup (Rbbox)
0.25	0.00	82.8/97.5/99.2/99.5	87.1/98.4/99.6/99.8
0.50	0.10	83.0/97.6/99.3/99.6	87.1/98.5/99.7/99.8
0.75	0.20	82.4/ 97.6/99.3/99.6	86.8/ 98.5/99.6/99.8

TABLE VI

THE IMPACT OF THE BLOCK-LABEL THRESHOLDS (DEFINED IN EQ. 15). THE TEST IS PERFORMED ON MVTec-AD USING AP, PRO, PIXEL-AUROC, AND IMAGE-AUROC METRICS IN BOTH UNSUPERVISED AND SUPERVISED SCENARIOS.

5 seconds and 17 seconds for labeling bounding boxes and block-wise labels on an image, respectively. In contrast, the SOTA method [36] based on pixel labels needs more than 32 seconds for labeling one image, while yielding consistently lower accuracy.

Recall that our block-labels are all converted from the pixel-labels based on two pre-defined parameters ϵ^+ and ϵ^- (Eq. 15), we carry out an experiment for verifying the model robustness on the fluctuation of these parameters. As the

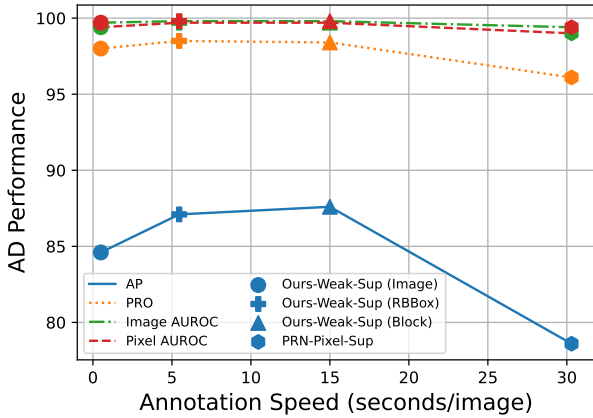


Fig. 6. The per-image annotation costs (x-axis) of the three levels of anomaly labels are shown as the circle (image label) plus (bounding-box label), triangle (block-wise label) and pentagon (pixel-wise label) shapes. The y-axis stands for the AD performances with the four metrics, shown as red-dashed (Pixel-AUROC), green-dashed (Image-AUROC), orange-dot (PRO) and blue-solid (AP) lines.

Perturb. (pixel)	Rbbox	Bbox
0	87.1/98.5/99.7/99.8	86.3/98.3/99.6/99.8
-3 ~ +3	86.7/98.5/99.6/99.8	86.2/98.3/99.6/99.7
-5 ~ +5	86.8/98.5/99.6/99.8	85.3/98.2/99.6/99.8
-7 ~ +7	86.0/98.4/99.6/99.8	85.9/98.2/99.6/99.8

TABLE VII

BOUNDING-BOX LABEL PERTURBATION ANALYSIS. THE FIRST COLUMN DENOTES THE SCALES OF THE PERTURBATION THE TEST IS CONDUCTED ON MVTEC AD WITH AP, PRO, PIXEL-AUROC, AND IMAGE-AUROC METRICS.

results shown in Tab. VI, the AD accuracies of WeakREST are generally stable when ϵ^+ and ϵ^- changes significantly.

Another concern about our weak labels might arise here is the proposed bounding-box labels are supposed to be annotated manually and thus the label noise is inevitable. In this sense, we test the proposed algorithm with perturbed bounding boxes and report the results in Tab. VII. From the table we can see that, even contaminated by the noise up to ± 7 pixels, which is around 15% of the average size of the bounding-boxes, the performance drop is still trivial: around 1% on AP while less than 0.2% for other metrics.

F. Ablation study

In this section, the most influential modules of WeakREST are evaluated in the manner of an ablation study. The involved modules include: the usage of Swin Transformer model introduced in Sec. III-C2 (Swin); the Position Constrained Feature defined in Sec. III-B2 (PCF); the PCA for faster matching described in Sec. III-B3 (PCA); the filtering process for reference images introduced in Sec. III-B4 (Filter); the foreground estimation proposed in Sec. III-E (Fore); the ResMixMatch algorithm introduced in Sec. III-D (ResMix); the randomly masking (Mask) and residual jittering (Jitter) augmentation strategy defined in Sec. III-C3. From the table we can see that most modules can improve the performance steadily except the “PCA” module which slightly reduce the AD performances. However, the accelerating module increase the running speed by around 28% (from 79.5 ms to 56.1 ms). The two accelerating module “PCA” and “Filter” can jointly

double the algorithm speed while keeping the accuracy nearly unchanged.

In addition, the impact of the backbone selection over Swin Transformer [42], ViT [55] and the UNet model employed in [32]) is illustrated in Table VIII. One can see that the combination of Swin Transformer achieves the best scores while the ViT model performs worst in the unsupervised condition, probably due to the model overfitting to the synthetic defects. However, when genuine defective samples become available in training, ViT surpasses UNet thanks to its higher capacity of feature extraction.

Finally, the performance of the proposed foreground estimation method (proposed in Sec. III-E) is evaluated in Tab. X, in terms of both accuracy and efficiency. From the table we can see that the proposed approach can almost consistently lift the AD scores, with a negligible additional complexity (0.3 ms). In contrast, to predict foreground regions directly on the test image will cost more computation (5.2 ms) while to treat the coresset sampling map (see Sec. III-E) as the foreground estimation can hardly increase the AD performances. When the traditional image binary method (employed in RealNet [83]) is used with WeakREST, the AD scores drop slightly.

V. CONCLUSION

In this paper, we propose to solve the AD problem via block-wise classifications, which require much less annotation effort than pixel-wise segmentation. To achieve this, a novel residual feature is designed to represent the anomaly status of image blocks. A swin transformer model, which is learned via a novel learning strategy, is employed to classify each block as defective or defect-free. The proposed two-stage algorithm achieves the new SOTA accuracy on three well-known AD datasets. In addition, when weaker labels such as bounding-boxes and image tags are used to roughly denote the defective regions, our ResMixMatch learning scheme can successfully exploit the information of unlabeled regions and achieve AD performances close to that with strong-supervisions. The proposed WeakREST algorithm brings record-breaking AD performances to the literature while only requiring much coarser annotations or, in short, **our WeakREST is cheaper in annotation and better in accuracy**.

Thus, this work paves a novel way to reduce the annotation cost for AD problems while maintaining accuracy. According to the experiment of this work, the weakly-supervised setting proposed in this work seems a more practical alternative to the supervised setting that limits the number of training images. In the future, we believe that better weakly-supervised AD algorithms will be developed by exploiting more useful information from the unlabeled image regions.

REFERENCES

- [1] S. Niu, B. Li, X. Wang, and Y. Peng, “Region-and strength-controllable gan for defect generation and segmentation in industrial images,” *IEEE Transactions on Industrial Informatics*, vol. 18, no. 7, pp. 4531–4541, 2021.
- [2] X. Ni, Z. Ma, J. Liu, B. Shi, and H. Liu, “Attention network for rail surface defect detection via consistency of intersection-over-union (iou)-guided center-point estimation,” *IEEE Transactions on Industrial Informatics*, vol. 18, no. 3, pp. 1694–1705, 2021.

Setting	Module							Performance					
	Swin	PCF	PCA	Filter	Fore	ResMix	Masks	Jitter	AP	PRO	P-AUROC	I-AUROC	Latency (ms)
Un	✓								66.2	95.0	97.6	96.7	65.4
	✓	✓							79.5	96.8	98.6	99.3	79.1
	✓	✓	✓						82.8	97.8	99.4	99.5	79.5
	✓	✓	✓	✓					82.1	97.7	99.3	99.4	56.1
	✓	✓	✓	✓	✓				82.6	97.7	99.3	99.3	39.4
	✓	✓	✓	✓	✓	✓			83.0	97.6	99.3	99.6	39.7
Rbbox	✓	✓	✓	✓	✓	✓	✓		83.1	97.6	99.3	99.7	39.7
	✓	✓	✓	✓	✓	✓	✓		85.8	98.3	99.6	99.7	39.7
	✓	✓	✓	✓	✓	✓	✓		86.8	98.4	99.6	99.7	39.7
	✓	✓	✓	✓	✓	✓	✓		87.1	98.5	99.7	99.8	39.7

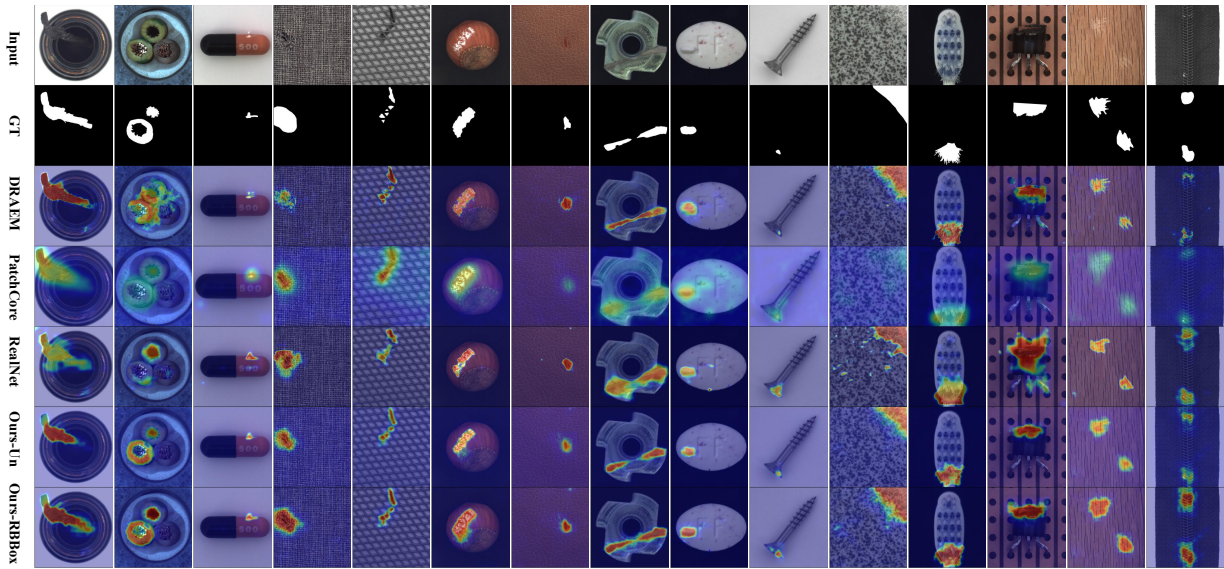
TABLE VIII
ABLATION STUDY RESULTS ON MVTEC AD.

Fig. 7. Qualitative results of our WeakREST on MVTec-AD, with the two levels of supervision: Un (unsupervised), Weak (Rbbox). Three unsupervised SOTA methods (RealNet [83], PatchCore [18] and DRAEM [50]) are also involved in the comparison.

Backbone	Unsupervised	Weak-sup (Rbbox)
Swin [42]	83.0/97.6/99.3/99.6	87.1/98.5/99.7/99.8
ViT [55]	75.7/94.0/98.5/99.3	80.5/96.8/99.0/99.3
DestSeg [32]	79.9/94.8/98.2/99.5	74.4/89.4/97.5/99.0

TABLE IX

EVALUATION ON BACKBONE SELECTION ON MVTEC AD ACROSS AP, PRO, PIXEL-AUROC, AND IMAGE-AUROC METRICS IN BOTH UNSUPERVISED AND WEAKLY-SUPERVISED SCENARIOS.

Foreground	Unsupervised	Weak-sup (Rbbox)	Latency (ms)
None	82.3/ 97.3/99.3 /99.2	86.4/ 98.2/99.6 /99.5	0
Ours	83.0/97.2/99.3/99.6	87.0/98.2/99.6/99.8	0.3
Ours (test image)	82.5/96.9/98.9/ 99.6	86.6/ 98.2/99.6/99.8	5.2
Coreset	82.3/96.6/99.0/99.5	86.4/ 98.2/99.6/99.8	0.3
Binarization [83]	80.0/93.0/96.8/99.5	85.4/96.1/98.2/ 99.8	0.4

TABLE X

COMPARING FOREGROUND ESTIMATION METHODS ON MVTEC AD (OBJECT CATEGORIES) ACROSS AP, PRO, PIXEL-AUROC, AND IMAGE-AUROC METRICS IN BOTH UNSUPERVISED AND WEAKLY-SUPERVISED SCENARIOS. NOTE THAT “NONE” STANDS FOR NO FOREGROUND INFORMATION IS USED. ALL THE METHODS GENERATE FOREGROUND MAPS AND THEN MERGED WITH THE RAW PREDICTION OF WEAKREST, AS DEFINED IN EQ. 20.

- [3] X. Tao, D. Zhang, W. Ma, Z. Hou, Z. Lu, and C. Adak, “Unsupervised anomaly detection for surface defects with dual-siamese network,” *IEEE Transactions on Industrial Informatics*, vol. 18, no. 11, pp. 7707–7717, 2022.
- [4] Y. Cao, X. Xu, Z. Liu, and W. Shen, “Collaborative discrepancy opti-

mization for reliable image anomaly localization,” *IEEE Transactions on Industrial Informatics*, pp. 1–10, 2023.

- [5] B. Cheng, Y. Wei, H. Shi, R. Feris, J. Xiong, and T. Huang, “Revisiting rcnn: On awakening the classification power of faster rcnn,” in *Proceedings of the European conference on computer vision (ECCV)*, 2018, pp. 453–468.
- [6] C.-Y. Wang, A. Bochkovskiy, and H.-Y. M. Liao, “Yolov7: Trainable bag-of-freebies sets new state-of-the-art for real-time object detectors,” *arXiv preprint arXiv:2207.02696*, 2022.
- [7] W. Wang, J. Dai, Z. Chen, Z. Huang, Z. Li, X. Zhu, X. Hu, T. Lu, L. Lu, H. Li *et al.*, “Internimage: Exploring large-scale vision foundation models with deformable convolutions,” *arXiv preprint arXiv:2211.05778*, 2022.
- [8] W. Wang, H. Bao, L. Dong, J. Bjorck, Z. Peng, Q. Liu, K. Aggarwal, O. K. Mohammed, S. Singhal, S. Som *et al.*, “Image as a foreign language: Beit pretraining for all vision and vision-language tasks,” *arXiv preprint arXiv:2208.10442*, 2022.
- [9] P. Bergmann, M. Fauser, D. Sattlegger, and C. Steger, “Mvtac ad—a comprehensive real-world dataset for unsupervised anomaly detection,” in *Proceedings of the IEEE/CVF conference on computer vision and pattern recognition*, 2019, pp. 9592–9600.
- [10] P. Mishra, R. Verk, D. Fornasier, C. Piciarelli, and G. L. Foresti, “Vt-adl: A vision transformer network for image anomaly detection and localization,” in *2021 IEEE 30th International Symposium on Industrial Electronics (ISIE)*. IEEE, 2021, pp. 01–06.
- [11] L. Ruff, R. Vandermeulen, N. Goernitz, L. Deecke, S. A. Siddiqui, A. Binder, E. Müller, and M. Kloft, “Deep one-class classification,” in *International conference on machine learning*. PMLR, 2018, pp. 4393–4402.
- [12] J. Yi and S. Yoon, “Patch svdd: Patch-level svdd for anomaly detection and segmentation,” in *Proceedings of the Asian Conference on Computer*

Vision, 2020.

[13] P. Liznerski, L. Ruff, R. A. Vandermeulen, B. J. Franks, M. Kloft, and K. R. Muller, “Explainable deep one-class classification,” in *International Conference on Learning Representations*, 2021. [Online]. Available: <https://openreview.net/forum?id=A5VV3UyIQz>

[14] F. V. Massoli, F. Falchi, A. Kantarci, S. Akti, H. K. Ekenel, and G. Amato, “Mocca: Multilayer one-class classification for anomaly detection,” *IEEE Transactions on Neural Networks and Learning Systems*, vol. 33, no. 6, pp. 2313–2323, 2021.

[15] T. Defard, A. Setkov, A. Loesch, and R. Audigier, “Padim: a patch distribution modeling framework for anomaly detection and localization,” in *Pattern Recognition. ICPR International Workshops and Challenges: Virtual Event, January 10–15, 2021, Proceedings, Part IV*. Springer, 2021, pp. 475–489.

[16] K. Zhang, B. Wang, and C.-C. J. Kuo, “Pedenet: Image anomaly localization via patch embedding and density estimation,” *Pattern Recognition Letters*, vol. 153, pp. 144–150, 2022.

[17] Y. Chen, Y. Tian, G. Pang, and G. Carneiro, “Deep one-class classification via interpolated gaussian descriptor,” in *Proceedings of the AAAI Conference on Artificial Intelligence*, vol. 36, 2022, pp. 383–392.

[18] K. Roth, L. Pemula, J. Zepeda, B. Schölkopf, T. Brox, and P. Gehler, “Towards total recall in industrial anomaly detection,” in *Proceedings of the IEEE/CVF Conference on Computer Vision and Pattern Recognition*, 2022, pp. 14318–14328.

[19] D. Kim, C. Park, S. Cho, and S. Lee, “Fapm: Fast adaptive patch memory for real-time industrial anomaly detection,” *arXiv preprint arXiv:2211.07381*, 2022.

[20] J. Bae, J.-H. Lee, and S. Kim, “Image anomaly detection and localization with position and neighborhood information,” *arXiv preprint arXiv:2211.12634*, 2022.

[21] R. Saiku, J. Sato, T. Yamada, and K. Ito, “Enhancing anomaly detection performance and acceleration,” *IEEJ Journal of Industry Applications*, vol. 11, no. 4, pp. 616–622, 2022.

[22] H. Zhu, Y. Kang, Y. Zhao, X. Yan, and J. Zhang, “Anomaly detection for surface of laptop computer based on patchcore gan algorithm,” in *2022 41st Chinese Control Conference (CCC)*. IEEE, 2022, pp. 5854–5858.

[23] G. Xie, J. Wang, J. Liu, Y. Jin, and F. Zheng, “Pushing the limits of fewshot anomaly detection in industry vision: Graphcore,” in *The Eleventh International Conference on Learning Representations*, 2023. [Online]. Available: <https://openreview.net/forum?id=xzmqxHdZAwO>

[24] B. Zong, Q. Song, M. R. Min, W. Cheng, C. Lumezanu, D. Cho, and H. Chen, “Deep autoencoding gaussian mixture model for unsupervised anomaly detection,” in *International conference on learning representations*, 2018.

[25] D. Dehaene and P. Eline, “Anomaly localization by modeling perceptual features,” *arXiv preprint arXiv:2008.05369*, 2020.

[26] Y. Shi, J. Yang, and Z. Qi, “Unsupervised anomaly segmentation via deep feature reconstruction,” *Neurocomputing*, vol. 424, pp. 9–22, 2021.

[27] J. Hou, Y. Zhang, Q. Zhong, D. Xie, S. Pu, and H. Zhou, “Divide-and-assemble: Learning block-wise memory for unsupervised anomaly detection,” in *Proceedings of the IEEE/CVF International Conference on Computer Vision*, 2021, pp. 8791–8800.

[28] J.-C. Wu, D.-J. Chen, C.-S. Fuh, and T.-L. Liu, “Learning unsupervised metaformer for anomaly detection,” in *Proceedings of the IEEE/CVF International Conference on Computer Vision*, 2021, pp. 4369–4378.

[29] M. Salehi, N. Sadjadi, S. Baselizadeh, M. H. Rohban, and H. R. Rabiee, “Multiresolution knowledge distillation for anomaly detection,” in *Proceedings of the IEEE/CVF conference on computer vision and pattern recognition*, 2021, pp. 14902–14912.

[30] H. Deng and X. Li, “Anomaly detection via reverse distillation from one-class embedding,” in *Proceedings of the IEEE/CVF Conference on Computer Vision and Pattern Recognition*, 2022, pp. 9737–9746.

[31] P. Bergmann, K. Batzner, M. Fauser, D. Sattlegger, and C. Steger, “Beyond dents and scratches: Logical constraints in unsupervised anomaly detection and localization,” *International Journal of Computer Vision*, vol. 130, no. 4, pp. 947–969, 2022.

[32] X. Zhang, S. Li, X. Li, P. Huang, J. Shan, and T. Chen, “Destseg: Segmentation guided denoising student-teacher for anomaly detection,” in *Proceedings of the IEEE/CVF Conference on Computer Vision and Pattern Recognition (CVPR)*, June 2023, pp. 3914–3923.

[33] C. Huang, H. Guan, A. Jiang, Y. Zhang, M. Spratling, and Y.-F. Wang, “Registration based few-shot anomaly detection,” in *Computer Vision–ECCV 2022: 17th European Conference, Tel Aviv, Israel, October 23–27, 2022, Proceedings, Part XXIV*. Springer, 2022, pp. 303–319.

[34] W. Liu, H. Chang, B. Ma, S. Shan, and X. Chen, “Diversity-measurable anomaly detection,” in *Proceedings of the IEEE/CVF Conference on Computer Vision and Pattern Recognition (CVPR)*, June 2023, pp. 12147–12156.

[35] C. Ding, G. Pang, and C. Shen, “Catching both gray and black swans: Open-set supervised anomaly detection,” in *Proceedings of the IEEE/CVF Conference on Computer Vision and Pattern Recognition*, 2022, pp. 7388–7398.

[36] H. Zhang, Z. Wu, Z. Wang, Z. Chen, and Y.-G. Jiang, “Prototypical residual networks for anomaly detection and localization,” in *Proceedings of the IEEE/CVF Conference on Computer Vision and Pattern Recognition (CVPR)*, June 2023, pp. 16281–16291.

[37] X. Yao, R. Li, J. Zhang, J. Sun, and C. Zhang, “Explicit boundary guided semi-push-pull contrastive learning for supervised anomaly detection,” in *Proceedings of the IEEE/CVF Conference on Computer Vision and Pattern Recognition (CVPR)*, June 2023, pp. 24490–24499.

[38] D. Tabernik, S. Šela, J. Skvarč, and D. Skočaj, “Segmentation-based deep-learning approach for surface-defect detection,” *Journal of Intelligent Manufacturing*, vol. 31, no. 3, pp. 759–776, 2020.

[39] Y. Huang, C. Qiu, and K. Yuan, “Surface defect saliency of magnetic tile,” *The Visual Computer*, vol. 36, pp. 85–96, 2020.

[40] J. Zhang, H. Su, W. Zou, X. Gong, Z. Zhang, and F. Shen, “Cadm: a weakly supervised learning-based category-aware object detection network for surface defect detection,” *Pattern Recognition*, vol. 109, p. 107571, 2021.

[41] J. Božič, D. Tabernik, and D. Skočaj, “Mixed supervision for surface-defect detection: From weakly to fully supervised learning,” *Computers in Industry*, vol. 129, p. 103459, 2021.

[42] Z. Liu, Y. Lin, Y. Cao, H. Hu, Y. Wei, Z. Zhang, S. Lin, and B. Guo, “Swin transformer: Hierarchical vision transformer using shifted windows,” in *Proceedings of the IEEE/CVF international conference on computer vision*, 2021, pp. 10012–10022.

[43] D. Berthelot, N. Carlini, I. Goodfellow, N. Papernot, A. Oliver, and C. A. Raffel, “Mixmatch: A holistic approach to semi-supervised learning,” *Advances in neural information processing systems*, vol. 32, 2019.

[44] M. Rudolph, B. Wandt, and B. Rosenhahn, “Same same but differnet: Semi-supervised defect detection with normalizing flows,” in *Proceedings of the IEEE/CVF winter conference on applications of computer vision*, 2021, pp. 1907–1916.

[45] J. Yu, Y. Zheng, X. Wang, W. Li, Y. Wu, R. Zhao, and L. Wu, “Fastflow: Unsupervised anomaly detection and localization via 2d normalizing flows,” *arXiv preprint arXiv:2111.07677*, 2021.

[46] M. Taitanian, A. Pardo, and P. Musé, “U-flow: A u-shaped normalizing flow for anomaly detection with unsupervised threshold,” *arXiv preprint arXiv:2211.12353*, 2022.

[47] J. Lei, X. Hu, Y. Wang, and D. Liu, “Pyramidflow: High-resolution defect contrastive localization using pyramid normalizing flow,” in *Proceedings of the IEEE/CVF Conference on Computer Vision and Pattern Recognition (CVPR)*, June 2023, pp. 14143–14152.

[48] L. Wu, D. Liu, W. Zhang, D. Chen, Z. Ge, F. Boussaid, M. Bennamoun, and J. Shen, “Pseudo-pair based self-similarity learning for unsupervised person re-identification,” *IEEE Transactions on Image Processing*, vol. 31, pp. 4803–4816, 2022.

[49] C.-L. Li, K. Sohn, J. Yoon, and T. Pfister, “Cutpaste: Self-supervised learning for anomaly detection and localization,” in *Proceedings of the IEEE/CVF Conference on Computer Vision and Pattern Recognition*, 2021, pp. 9664–9674.

[50] V. Zavrtanik, M. Kristan, and D. Skočaj, “Draem-a discriminatively trained reconstruction embedding for surface anomaly detection,” in *Proceedings of the IEEE/CVF International Conference on Computer Vision*, 2021, pp. 8330–8339.

[51] M. Yang, P. Wu, and H. Feng, “Memseg: A semi-supervised method for image surface defect detection using differences and commonalities,” *Engineering Applications of Artificial Intelligence*, vol. 119, p. 105835, 2023.

[52] J. Deng, W. Dong, R. Socher, L.-J. Li, K. Li, and L. Fei-Fei, “Imagenet: A large-scale hierarchical image database,” in *2009 IEEE conference on computer vision and pattern recognition*. Ieee, 2009, pp. 248–255.

[53] O. Russakovsky, J. Deng, H. Su, J. Krause, S. Satheesh, S. Ma, Z. Huang, A. Karpathy, A. Khosla, M. Bernstein *et al.*, “Imagenet large scale visual recognition challenge,” *International journal of computer vision*, vol. 115, pp. 211–252, 2015.

[54] G. Zhang, K. Cui, T.-Y. Hung, and S. Lu, “Defect-gan: High-fidelity defect synthesis for automated defect inspection,” in *Proceedings of the IEEE/CVF Winter Conference on Applications of Computer Vision*, 2021, pp. 2524–2534.

[55] A. Dosovitskiy, L. Beyer, A. Kolesnikov, D. Weissenborn, X. Zhai, T. Unterthiner, M. Dehghani, M. Minderer, G. Heigold, S. Gelly *et al.*,

“An image is worth 16x16 words: Transformers for image recognition at scale,” in *International Conference on Learning Representations*, 2021.

[56] Z. Liu, H. Hu, Y. Lin, Z. Yao, Z. Xie, Y. Wei, J. Ning, Y. Cao, Z. Zhang, L. Dong, F. Wei, and B. Guo, “Swin transformer v2: Scaling up capacity and resolution,” in *Proceedings of the IEEE/CVF Conference on Computer Vision and Pattern Recognition (CVPR)*, June 2022, pp. 12 009–12 019.

[57] S. Huang, Z. Lu, R. Cheng, and C. He, “Fapn: Feature-aligned pyramid network for dense image prediction,” in *Proceedings of the IEEE/CVF international conference on computer vision*, 2021, pp. 864–873.

[58] A. Hatamizadeh, V. Nath, Y. Tang, D. Yang, H. R. Roth, and D. Xu, “Swin unetr: Swin transformers for semantic segmentation of brain tumors in mri images,” in *Brainlesion: Glioma, Multiple Sclerosis, Stroke and Traumatic Brain Injuries: 7th International Workshop, BrainLes 2021, Held in Conjunction with MICCAI 2021, Virtual Event, September 27, 2021, Revised Selected Papers, Part I*. Springer, 2022, pp. 272–284.

[59] H. Cao, Y. Wang, J. Chen, D. Jiang, X. Zhang, Q. Tian, and M. Wang, “Swin-unet: Unet-like pure transformer for medical image segmentation,” in *Computer Vision–ECCV 2022 Workshops: Tel Aviv, Israel, October 23–27, 2022, Proceedings, Part III*. Springer, 2023, pp. 205–218.

[60] B. Dong, F. Zeng, T. Wang, X. Zhang, and Y. Wei, “Solq: Segmenting objects by learning queries,” *Advances in Neural Information Processing Systems*, vol. 34, pp. 21 898–21 909, 2021.

[61] F. Li, H. Zhang, S. Liu, L. Zhang, L. M. Ni, H.-Y. Shum *et al.*, “Mask dino: Towards a unified transformer-based framework for object detection and segmentation,” *arXiv preprint arXiv:2206.02777*, 2022.

[62] K. Ying, Q. Zhong, W. Mao, Z. Wang, H. Chen, L. Y. Wu, Y. Liu, C. Fan, Y. Zhuge, and C. Shen, “Consistent training for online video instance segmentation,” in *Proceedings of the IEEE/CVF international conference on computer vision*, 2023, pp. 899–908.

[63] M. Xu, Z. Zhang, H. Hu, J. Wang, L. Wang, F. Wei, X. Bai, and Z. Liu, “End-to-end semi-supervised object detection with soft teacher,” in *Proceedings of the IEEE/CVF International Conference on Computer Vision*, 2021, pp. 3060–3069.

[64] X. Dai, Y. Chen, B. Xiao, D. Chen, M. Liu, L. Yuan, and L. Zhang, “Dynamic head: Unifying object detection heads with attentions,” in *Proceedings of the IEEE/CVF conference on computer vision and pattern recognition*, 2021, pp. 7373–7382.

[65] T. Liang, X. Chu, Y. Liu, Y. Wang, Z. Tang, W. Chu, J. Chen, and H. Ling, “Cbnnet: A composite backbone network architecture for object detection,” *IEEE Transactions on Image Processing*, vol. 31, pp. 6893–6906, 2022.

[66] H. Üzen, M. Türkoğlu, B. Yanikoglu, and D. Hanbay, “Swin-mfinet: Swin transformer based multi-feature integration network for detection of pixel-level surface defects,” *Expert Systems with Applications*, vol. 209, p. 118269, 2022.

[67] L. Gao, J. Zhang, C. Yang, and Y. Zhou, “Cas-vswin transformer: A variant swin transformer for surface-defect detection,” *Computers in Industry*, vol. 140, p. 103689, 2022.

[68] X. Zhu and A. B. Goldberg, “Introduction to semi-supervised learning,” *Synthesis lectures on artificial intelligence and machine learning*, vol. 3, no. 1, pp. 1–130, 2009.

[69] D. Berthelot, N. Carlini, E. D. Cubuk, A. Kurakin, K. Sohn, H. Zhang, and C. Raffel, “Remixmatch: Semi-supervised learning with distribution alignment and augmentation anchoring,” *arXiv preprint arXiv:1911.09785*, 2019.

[70] K. Sohn, D. Berthelot, N. Carlini, Z. Zhang, H. Zhang, C. A. Raffel, E. D. Cubuk, A. Kurakin, and C.-L. Li, “Fixmatch: Simplifying semi-supervised learning with consistency and confidence,” *Advances in neural information processing systems*, vol. 33, pp. 596–608, 2020.

[71] Y. Wang, H. Chen, Q. Heng, W. Hou, Y. Fan, Z. Wu, J. Wang, M. Savvides, T. Shinoda, B. Raj, B. Schiele, and X. Xie, “Freematch: Self-adaptive thresholding for semi-supervised learning,” in *The Eleventh International Conference on Learning Representations, 2023*. [Online]. Available: https://openreview.net/forum?id=PDruPTXJI_A

[72] L. Wu, R. Hong, Y. Wang, and M. Wang, “Cross-entropy adversarial view adaptation for person re-identification,” *IEEE Transactions on Circuits and Systems for Video Technology*, vol. 30, pp. 2081–2020, 2020.

[73] H. Zhang, M. Cisse, Y. N. Dauphin, and D. Lopez-Paz, “mixup: Beyond empirical risk minimization,” in *International Conference on Learning Representations*, 2018. [Online]. Available: <https://openreview.net/forum?id=r1Ddp1-Rb>

[74] S. Yun, D. Han, S. J. Oh, S. Chun, J. Choe, and Y. Yoo, “Cutmix: Regularization strategy to train strong classifiers with localizable features,” in *Proceedings of the IEEE/CVF international conference on computer vision*, 2019, pp. 6023–6032.

[75] C.-C. Hsu, K.-J. Hsu, C.-C. Tsai, Y.-Y. Lin, and Y.-Y. Chuang, “Weakly supervised instance segmentation using the bounding box tightness prior,” *Advances in Neural Information Processing Systems*, vol. 32, 2019.

[76] H. Kervadec, J. Dolz, S. Wang, E. Granger, and I. B. Ayed, “Bounding boxes for weakly supervised segmentation: Global constraints get close to full supervision,” in *Medical imaging with deep learning*. PMLR, 2020, pp. 365–381.

[77] J. Lee, J. Yi, C. Shin, and S. Yoon, “Bbam: Bounding box attribution map for weakly supervised semantic and instance segmentation,” in *Proceedings of the IEEE/CVF conference on computer vision and pattern recognition*, 2021, pp. 2643–2652.

[78] D. Gudovskiy, S. Ishizaka, and K. Kozuka, “Cflow-ad: Real-time unsupervised anomaly detection with localization via conditional normalizing flows,” in *Proceedings of the IEEE/CVF Winter Conference on Applications of Computer Vision*, 2022, pp. 98–107.

[79] K. He, X. Chen, S. Xie, Y. Li, P. Dollár, and R. Girshick, “Masked autoencoders are scalable vision learners,” in *Proceedings of the IEEE/CVF Conference on Computer Vision and Pattern Recognition*, 2022, pp. 16 000–16 009.

[80] T.-Y. Lin, P. Goyal, R. Girshick, K. He, and P. Dollár, “Focal loss for dense object detection,” in *Proceedings of the IEEE international conference on computer vision*, 2017, pp. 2980–2988.

[81] C. Shorten and T. M. Khoshgoftaar, “A survey on image data augmentation for deep learning,” *Journal of big data*, vol. 6, no. 1, pp. 1–48, 2019.

[82] S. Yang, W. Xiao, M. Zhang, S. Guo, J. Zhao, and F. Shen, “Image data augmentation for deep learning: A survey,” *arXiv preprint arXiv:2204.08610*, 2022.

[83] X. Zhang, M. Xu, and X. Zhou, “Realnet: A feature selection network with realistic synthetic anomaly for anomaly detection,” in *Proceedings of the IEEE/CVF Conference on Computer Vision and Pattern Recognition*, 2024, pp. 16 699–16 708.

[84] S. Zagoruyko and N. Komodakis, “Wide residual networks,” *arXiv preprint arXiv:1605.07146*, 2016.

[85] N.-C. Ristea, N. Madan, R. T. Ionescu, K. Nasrollahi, F. S. Khan, T. B. Moeslund, and M. Shah, “Self-supervised predictive convolutional attentive block for anomaly detection,” in *Proceedings of the IEEE/CVF Conference on Computer Vision and Pattern Recognition*, 2022, pp. 13 576–13 586.

[86] Z. Liu, Y. Zhou, Y. Xu, and Z. Wang, “Simplenet: A simple network for image anomaly detection and localization,” in *Proceedings of the IEEE/CVF Conference on Computer Vision and Pattern Recognition (CVPR)*, June 2023, pp. 20 402–20 411.

[87] T. D. Tien, A. T. Nguyen, N. H. Tran, T. D. Huy, S. T. Duong, C. D. T. Nguyen, and S. Q. H. Truong, “Revisiting reverse distillation for anomaly detection,” in *Proceedings of the IEEE/CVF Conference on Computer Vision and Pattern Recognition (CVPR)*, June 2023, pp. 24 511–24 520.

[88] G. Pang, C. Ding, C. Shen, and A. v. d. Hengel, “Explainable deep few-shot anomaly detection with deviation networks,” *arXiv preprint arXiv:2108.00462*, 2021.

[89] J. Zhu, C. Ding, Y. Tian, and G. Pang, “Anomaly heterogeneity learning for open-set supervised anomaly detection,” in *Proceedings of the IEEE/CVF Conference on Computer Vision and Pattern Recognition*, 2024, pp. 17 616–17 626.

[90] T. Cheng, X. Wang, S. Chen, Q. Zhang, and W. Liu, “Boxteacher: Exploring high-quality pseudo labels for weakly supervised instance segmentation,” in *Proceedings of the IEEE/CVF Conference on Computer Vision and Pattern Recognition*, 2023, pp. 3145–3154.

[91] P. Bergmann, M. Fauser, D. Sattlegger, and C. Steger, “Uninformed students: Student-teacher anomaly detection with discriminative latent embeddings,” in *Proceedings of the IEEE/CVF conference on computer vision and pattern recognition*, 2020, pp. 4183–4192.

[92] J. Chibane, F. Engelmann, T. Anh Tran, and G. Pons-Moll, “Box2mask: Weakly supervised 3d semantic instance segmentation using bounding boxes,” in *European conference on computer vision*. Springer, 2022, pp. 681–699.